Flow Turbulence Combust (2016) 96:45–93
DOI 10.1007/s10494-015-9648-7

# Reynolds-Stress Model Prediction of 3-D Duct Flows

**G. A. Gerolymos**[1] · **I. Vallet**[1]

Received: 3 December 2014 / Accepted: 6 August 2015 / Published online: 2 October 2015

**Abstract** The paper examines the impact of different modelling choices in second-moment closures by assessing model performance in predicting 3-D duct flows. The test-cases (developing flow in a square duct (Gessner and Emery, ASME J. Fluids Eng. **103**, 445–455, 1981), circular-to-rectangular transition-duct (Davis and Gessner, AIAA J. **30**, 367–375, 1992), and S-duct with large separation (Wellborn et al., J. Prop. Power **10**, 668–675 1994) include progressively more complex strains. Comparison of experimental data with selected 7-equation models (6 Reynolds-stress-transport and 1 scale-determining equations), which differ in the closure of the velocity/pressure-gradient tensor $\Pi_{ij}$, suggests that rapid redistribution controls separation and secondary-flow prediction, whereas, inclusion of pressure-diffusion modelling improves reattachment and relaxation behaviour.

**Keywords** Turbulence modelling · Reynolds stress model · Second moment closure · Separated flow · Secondary flow · 3-D duct flows

## 1 Introduction

The accurate prediction of 3-D turbulent flow in geometrically complex ducts is important in many practical applications, including aerospace [26], process [4] and nuclear [11] engineering, and agrofood industry [3]. These flows can be particularly complex, and tur-

---

✉ I. Vallet
isabelle.vallet@upmc.fr

G. A. Gerolymos
georges.gerolymos@upmc.fr

[1] Sorbonne Universités, Université Pierre-et-Marie-Curie (UPMC), 4 Place Jussieu, 75005 Paris, France

bulence structure may be influenced by various mechanisms, including 3-D boundary-layer entrainment [50], secondary flows [8], flow separation [69], especially 3-D [21], and important streamline curvature [71], associated with the presence of convex and concave bends [70]. Therefore, in a RANS (Reynolds-averaged Navier-Stokes) framework [65], differential full Reynolds-stress models (RSMs) are an appropriate choice [45], in an effort to include terms in the model that account for all these mechanisms, especially if one considers not only the prediction of the mean flow, but also of the detailed Reynolds-stress field [83]. In a recent study [26] of a double-S-shaped duct intake, typical of unmanned combat air vehicles (UCAVs), comparison of RSM predictions with available measurements highlighted the importance of the closure for the rapid part of the velocity/pressure-gradient tensor $\Pi_{ij} := -\overline{u'_i\partial_{x_j}p'} - \overline{u'_j\partial_{x_i}p'}$ (where $u_i \in \{u, v, w\}$ are the velocity-components in the Cartesian frame $x_i \in \{x, y, z\}$, $p$ is the pressure, $\overline{(\cdot)}$ denotes Reynolds (ensemble) averaging, and $(\cdot)'$ denotes Reynolds-fluctuations) in successfully predicting the complex 3-D flow structure dominated by 2 pairs of contrarotating streamwise vortices.

To improve our understanding of the predictive capability, but also of limitations, of RSMs applied to the computation of streamwise-developing 3-D duct flows, it seemed worthwhile to study 3 configurations, where the effects of different mechanisms could be assessed separately, or at least sequentially: (a) developing flow in a square duct [39], (b) flow in a circular-to-rectangular (C-to-R) transition duct [19], and (c) separated flow in a circular diffusing S-duct [80]. These are highly anisotropic and inhomogeneous 3-D flows, driven by mechanisms that are not modelled in linear eddy-viscosity closures, and are therefore well suited for the assessment of anisotropy-resolving closures [53].

In turbulent fully-developed (streamwise-invariant in the mean) flow in a straight square duct [40] the anisotropy of the diagonal stresses, $\overline{v'^2}$ and $\overline{w'^2}$, in the crossflow plane $yz$ [8], but also the inhomogeneity of the gradients of the secondary shear-stress $\overline{v'w'}$ [9, (3), p. 378], trigger secondary ($\perp x$) flow, associated with streamwise vorticity [9]. The Gessner and Emery [39] test-case is further complicated by the streamwise evolution of the very thin inflow boundary-layers, on the duct walls, which grow streamwise, until they interact and fill the entire duct, resulting in fully-developed (streamwise-invariant in the mean) flow. Previous RSM computations of this flow [29, 72, 77] illustrated the difficulty to correctly predict the streamwise development of the centerline velocity $\bar{u}_{\mathrm{CL}}$, but also, near the duct's exit where the flow reaches a fully-developed state, the underestimation of the secondary velocity along the corner bisector (diagonal); this underestimation of the secondary-flow velocities is also observed in fully-developed flow predictions [63]. Notice that, in fully-developed turbulent square-duct flow, secondary ”*velocities $\cdots$ are found to be smaller than the root-mean-square turbulent velocity*” [9, p. 376], and, furthermore, ”*secondary-flow velocities, when nondimensionalized with either the bulk velocity ($\bar{u}_{\mathrm{B}}$) or the axial mean-flow velocity at the channel centerline ($\bar{u}_{\mathrm{CL}}$) decrease for an increase in Reynolds number*” [40, p. 689]. The So-Yuan [72] wall-normal-free (WNF) RSM slightly underestimates the centerline velocity peak [72, Fig. 14, p. 51], while results with different WNF-RSM variants [29, 77] demonstrated the sensitivity of the prediction of the $x$-wise development of $\bar{u}_{\mathrm{CL}}$ to the closures for both $\Pi_{ij}$ [29] and turbulent diffusion [77]. Finally, the wall-geometry-dependent Launder-Shima [52] RSM was found to perform poorly for this type of flows [29], despite a slight improvement when using its WNF version.

Contrary to turbulence-driven secondary flows [8, Prandtl's second kind], pressure-driven secondary flows [8, Prandtl's first kind] are generally much stronger [22]. In the C-to-R transition duct studied by Davis and Gessner [19], the curvature of the walls in the transition part of the duct induces pressure-gradients in the crossflow plane $yz$ [19, Fig. 14,

p. 373], driving relatively strong secondary flows that develop into 2 contrarotating vortex pairs. The cross-sectional area of the duct varies in the divergent/convergent transition part of the duct [54, Fig. 4, p. 242], and this further complicates the flow, although the diverging part of the duct was sufficiently long to exclude separation [19]. Previous RSM computations for this configuration were reported by Sotiropoulos and Patel [73] with a variant of the Launder-Shima [52] RSM, by Lien and Leschziner [54] with a zonal Gibson-Launder [42] RSM coupled with a nonlinear k-$\varepsilon$ model near the wall, and by Craft and Launder [15] with their two-component limit (TCL) RSM. The detailed comparisons of model predictions with available experimental measurements presented in [73] showed quite satisfactory agreement, both for the mean-flow and for the Reynolds-stresses, with the single exception of the Reynolds-stresses at the last measurement station, located 2 inlet diameters downstream of the end of the C-to-R transition, where computations do not predict the measured increase of turbulence levels, compared to the previous measurement station located exactly at the end of the C-to-R transition.

The diffusing S-duct, that was experimentally investigated by Wellborn et al. [80], combines centerline curvature and cross-sectional area increase, both of which induce streamline curvature, with associated crossflow pressure-gradients which generate significant secondary flows. This configuration is further complicated by the strong adverse streamwise pressure-gradient, related to the streamwise-diverging cross-sectional area of the duct, which induces a large separated-flow zone. The presence of several interacting mechanisms renders this test-case a difficult challenge, even for the prediction of the mean-flow velocity and total-pressure fields [47]. Previous RSM computations were reported by Vallet [77], who found that the predictive quality of the models depended mainly on the ability of the redistribution closure to correctly predict separation.

The second-moment closure (SMC) that was assessed in the present work is the RSM developed by Gerolymos et al. [28] (hereafter GLVY RSM), which is the final result of previous research [29, 35, 66, 77] on the development of wall-normal-free (WNF) RSMs with quasi-linear closure for the rapid part of $\Pi_{ij}$. To put the comparisons with measurements into perspective, results were also presented for the RSM developed by Gerolymos and Vallet [35] (hereafter GV RSM), the wall-normal-free version of the Launder-Shima [52] RSM with the Launder-Sharma [51] closure for the modified dissipation-rate [29] (hereafter WNF–LSS RSM), and with the baseline Launder-Sharma k-$\varepsilon$ model [51] (hereafter LS k–$\varepsilon$). All of the computations were run specifically for the present assessment, carefully adjusting the boundary-conditions separately for each model, to obtain the best possible match with the experimental data at the first available measurement plane.

The RSMs used in the present work are briefly reviewed in Section 2, with particular emphasis on differences between modelling choices, and their implications. In Section 3 computational results using the various models are compared with available experimental measurements. Conclusions from the present results, and recommendations for future research, are summarized in Section 4.

## 2 Turbulence Closures and Flow Solver

All measurements were performed in airflow, and a compressible aerodynamic solver was used in the computations. The square [39, $\bar{M}_{\text{CL}} \sim 0.05$] and C-to-R [19, $\bar{M}_{\text{CL}} \sim 0.1$] ducts test-cases were at sufficiently low Mach-number for the flow to be essentially incompressible ($\bar{M}_{\text{CL}}$ is a typical centerline Mach number), whereas in the S-duct high-subsonic flow conditions prevail [80, $\bar{M}_{\text{CL}} \sim 0.6$]. Obviously in all of the previous cases, density fluctuations have negligible influence [7], so that Favre (used in Section 2.1) or Reynolds averages are, for practical purposes, equivalent. The flow is modelled by the Reynolds-averaged Navier-Stokes (RANS) equations [35, 78], coupled with the appropriate modelled turbulence-transport equations (Sections 2.1 and 2.2). All computations were performed for air thermodynamics [78].

### 2.1 Turbulence closures

Details on the development of the RSMs used in the present work, can be found in the original papers [28, 29, 35]. They are summarized below for completeness, in a common representation which highlights differences in the closure choices between different models. Define

$$r_{ij} := \frac{1}{\bar{\rho}}\overline{\rho u_i'' u_j''} \;\; ; \;\; \mathrm{k} := \tfrac{1}{2} r_{\ell\ell} \;\; ; \;\; a_{ij} := \frac{r_{ij}}{\mathrm{k}} - \tfrac{2}{3}\delta_{ij} \tag{1a}$$

$$A_2 := a_{ik}a_{ki} \;\; ; \;\; A_3 := a_{ik}a_{kj}a_{ji} \;\; ; \;\; A := 1 - \tfrac{9}{8}(A_2 - A_3) \tag{1b}$$

$$\varepsilon^* := \varepsilon - 2\breve{\nu}\frac{\partial\sqrt{\mathrm{k}}}{\partial x_\ell}\frac{\partial\sqrt{\mathrm{k}}}{\partial x_\ell} \;\; ; \;\; \ell_{\mathrm{T}} := \frac{\mathrm{k}^{\frac{3}{2}}}{\varepsilon} \;\; ; \;\; \ell_{\mathrm{T}}^* := \frac{\mathrm{k}^{\frac{3}{2}}}{\varepsilon^*} \;\; ; \;\; Re_{\mathrm{T}} := \frac{\mathrm{k}^2}{\breve{\nu}\varepsilon} \;\; ; \;\; Re_{\mathrm{T}}^* := \frac{\mathrm{k}^2}{\breve{\nu}\varepsilon^*} \tag{1c}$$

$$\breve{\mu} := \mu_{\mathrm{Sutherland}}(\tilde{T}) \;\; ; \;\; \breve{\nu} := \frac{\breve{\mu}}{\bar{\rho}} \;\; ; \;\; \breve{S}_{ij} := \tfrac{1}{2}\left(\frac{\partial\tilde{u}_i}{\partial x_j} + \frac{\partial\tilde{u}_j}{\partial x_i}\right) \tag{1d}$$

where $\rho$ is the density, $r_{ij}$ are the 2-moments of velocity-fluctuations, k is the turbulent kinetic energy, $\delta_{ij}$ is the identity tensor, $a_{ij}$ is the deviatoric Reynolds-stress anisotropy-tensor, with invariants $A_2$ and $A_3$, $A$ is Lumley's [55] flatness parameter, $\varepsilon$ is the dissipation-rate of k, $\varepsilon^*$ is the modified dissipation-rate [51], $\ell_{\mathrm{T}}$ ($\ell_{\mathrm{T}}^*$) is the turbulent lengthscale and $Re_{\mathrm{T}}$ ($Re_{\mathrm{T}}^*$) is the turbulent Reynolds-number, (defined using either $\varepsilon$ or $\varepsilon^*$), $\breve{\mu}$ is the dynamic viscosity evaluated from Sutherland's law [78, (6), p. 528] at mean temperature $\tilde{T}$, $\breve{\nu}$ is the kinematic viscosity at mean-flow conditions, $\breve{S}_{ij}$ is the deformation-rate tensor of the mean-velocity field, $\widetilde{(\cdot)}$ denotes Favre averaging, $(\cdot)''$ are Favre fluctuations, and $\breve{(\cdot)}$ denotes a function of averaged quantities that cannot be identified with a Reynolds or a Favre average [34, 38]. Recall that $\varepsilon$ and $\varepsilon^*$ are significantly different only very near the wall [34, 35, 51].

All of the 3 RSMs [28, 29, 35] use the same scale-determining equation, solving for the modified dissipation-rate $\varepsilon^*$ [35, 51]

$$\begin{aligned}\frac{\partial\bar{\rho}\varepsilon^*}{\partial t} + \frac{\partial\left(\bar{\rho}\varepsilon^*\tilde{u}_\ell\right)}{\partial x_\ell} &= \frac{\partial}{\partial x_\ell}\left[C_\varepsilon\frac{\mathrm{k}}{\varepsilon^*}\bar{\rho}r_{m\ell}\frac{\partial\varepsilon^*}{\partial x_m} + \breve{\mu}\frac{\partial\varepsilon^*}{\partial x_\ell}\right] \\ &\quad + C_{\varepsilon_1}P_{\mathrm{k}}\frac{\varepsilon^*}{\mathrm{k}} - C_{\varepsilon_2}\bar{\rho}\frac{\varepsilon^{*2}}{\mathrm{k}} + 2\breve{\mu}C_\mu\frac{\mathrm{k}^2}{\varepsilon^*}\frac{\partial^2\tilde{u}_i}{\partial x_\ell\partial x_\ell}\frac{\partial^2\tilde{u}_i}{\partial x_m\partial x_m}\end{aligned} \tag{2a}$$

$$P_{\mathrm{k}} := \tfrac{1}{2}P_{\ell\ell} \;\; ; \;\; C_\varepsilon = 0.18 \;\; ; \;\; C_{\varepsilon 1} = 1.44 \tag{2b}$$

$$C_{\varepsilon 2} = 1.92(1 - 0.3\mathrm{e}^{-Re_{\mathrm{T}}^{*2}}) \;\; ; \;\; C_\mu = 0.09\mathrm{e}^{-\frac{3.4}{(1+0.02Re_{\mathrm{T}}^*)^2}} \tag{2c}$$

where $t$ is the time, $P_{ij}$ is the Reynolds-stress production-tensor (3) and $P_\mathrm{k}$ is the production-rate of turbulent kinetic energy k. The scale-determining (2) is solved along with the 6 transport equations for the components of the symmetric tensor $r_{ij}$ [28, (1), p. 2849]

$$\underbrace{\frac{\partial}{\partial t}\left(\bar{\rho} r_{ij}\right)+\frac{\partial}{\partial x_\ell}\left(\bar{\rho} r_{ij}\tilde{u}_\ell\right)}_{C_{ij}}=\underbrace{-\bar{\rho} r_{i\ell}\frac{\partial \tilde{u}_j}{\partial x_\ell}-\bar{\rho} r_{j\ell}\frac{\partial \tilde{u}_i}{\partial x_\ell}}_{P_{ij}}+\underbrace{\frac{\partial}{\partial x_\ell}\left(\breve{\mu}\frac{\partial r_{ij}}{\partial x_\ell}\right)}_{d_{ij}^{(\mu)}}$$
$$+\ d_{ij}^{(u)}+\Pi_{ij}-\bar{\rho}\varepsilon_{ij}+K_{ij} \tag{3}$$

where convection $C_{ij}$, production $P_{ij}$ and viscous diffusion $d_{ij}^{(\mu)}$ are computable terms, and diffusion by the fluctuating velocity field $d_{ij}^{(u)}$, the velocity/pressure-gradient correlation $\Pi_{ij}$, the dissipation-tensor $\varepsilon_{ij}$ and the fluctuating-density terms $K_{ij}$ require closure. For all of the 3 RSMs [28, 29, 35] the fluctuating-density terms $K_{ij}$ and the pressure-dilatation correlation $\phi_p := \overline{p'\partial_{x_\ell} u'_\ell}$ [28, (1), p. 2849] were neglected

$$K_{ij}=0 \qquad ; \qquad \phi_p=0 \tag{4}$$

this being a safe assumption for the subsonic flows that were investigated [19, 39, 80]. The closure for the remaining terms ($d_{ij}^{(u)}$, $\Pi_{ij}$, $\varepsilon_{ij}$) differs between the 3 RSMs [28, 29, 35], either in the functional dependence of the model coefficients on the local turbulent scales, or in the tensorial representation that was used (Table 1).

Diffusion by the triple velocity correlation

$$d_{ij}^{(u)} := \frac{\partial}{\partial x_\ell}\left(-\overline{\rho u''_i u''_j u''_\ell}\right) \tag{5}$$

is modelled (Table 1) using either the Daly-Harlow [17] closure in the WNF–LSS RSM [29], or the Hanjalić-Launder [46] closure in the GV [35] and GLVY [28] RSMs.

The dissipation-rate tensor is modelled as

$$\bar{\rho}\varepsilon_{ij}=\frac{2}{3}\bar{\rho}\varepsilon\left(1-f_\varepsilon\right)\delta_{ij}+f_\varepsilon\frac{\varepsilon}{\mathrm{k}}\bar{\rho} r_{ij} \tag{6}$$

The anisotropic part modelled via $f_\varepsilon$ (Table 1) is only present in the GLVY RSM, the GV and WNF–LSS RSMs following Lumley's [55] suggestion to include the anisotropy of $\varepsilon_{ij}$ in the closure for the slow-redistribution terms [27].

**Table 1** Coefficients in the closure relations (5–7), for the GLVY [28], the GV [35], and the WNF–LSS [29] RSMs

| Eq. | Term | GLVY | GV | WNF–LSS |
|---|---|---|---|---|
| (5) | $-\overline{\rho u_i'' u_j'' u_k''}$ | $C^{(\mathrm{S}u)} \frac{\mathrm{k}}{\varepsilon} \left( \bar{\rho} r_{im} \frac{\partial r_{jk}}{\partial x_m} + \bar{\rho} r_{jm} \frac{\partial r_{ki}}{\partial x_m} + \bar{\rho} r_{km} \frac{\partial r_{ij}}{\partial x_m} \right)$ | | $C^{(\mathrm{S}u)} \frac{\mathrm{k}}{\varepsilon} \bar{\rho} r_{km} \frac{\partial r_{ij}}{\partial x_m}$ |
| | $C^{(\mathrm{S}u)}$ | 0.11 | 0.11 | 0.22 |
| (6) | $f_\varepsilon$ | $1 - A^{[1+A^2]} \left[ 1 - \mathrm{e}^{-\frac{Re_\mathrm{T}}{10}} \right]$ | 0 | 0 |
| (7b) | $C^{(\mathrm{Sp1})}$ | $-0.005$ | 0 | 0 |
| (7b) | $C^{(\mathrm{Sp2})}$ | $+0.022$ | 0 | 0 |
| (7b) | $C^{(\mathrm{Rp})}$ | $-0.005$ | 0 | 0 |
| (7d) | $C_\phi^{(\mathrm{RH})}$ | $\min\left[1, 0.75 + 1.3 \max\left[0, A - 0.55\right]\right] A^{[\max(0.25, 0.5 - 1.3 \max[0, A - 0.55])]} \left[ 1 - \max\left(0, 1 - \frac{Re_\mathrm{T}}{50}\right) \right]$ | | $0.75\sqrt{A}$ |
| (7d) | $C_\phi^{(\mathrm{RI})}$ | $\max\left[ \frac{2}{3} - \frac{1}{6 C_\phi^{(\mathrm{RH})}}, 0 \right] \left\lvert \mathrm{grad} \left( \frac{\ell_\mathrm{T} \left[ 1 - \mathrm{e}^{-\frac{Re_\mathrm{T}^*}{30}} \right]}{1 + 1.6 A_2^{\max(0.6, A)}} \right) \right\rvert$ | $\max\left[ \frac{2}{3} - \frac{1}{6 C_\phi^{(\mathrm{RH})}}, 0 \right] \left\lvert \mathrm{grad} \left( \frac{\ell_\mathrm{T} \left[ 1 - \mathrm{e}^{-\frac{Re_\mathrm{T}^*}{30}} \right]}{1 + 1.8 A_2^{\max(0.6, A)}} \right) \right\rvert$ | |
| (7e) | $\varepsilon_\mathrm{V}$ | $\varepsilon^*$ | $\varepsilon$ | $\varepsilon$ |
| (7e) | $C_\phi^{(\mathrm{SH1})}$ | $3.7 A A_2^{\frac{1}{4}} \left[ 1 - \mathrm{e}^{-\left(\frac{Re_\mathrm{T}}{130}\right)^2} \right]$ | $1 + 2.58 A A_2^{\frac{1}{4}} \left[ 1 - \mathrm{e}^{-(\frac{Re_\mathrm{T}}{150})^2} \right]$ | |
| (7e) | $C_\phi^{(\mathrm{SI1})}$ | $\left[ -\frac{4}{9} \left( C_\phi^{(\mathrm{SH1})} - \frac{9}{4} \right) \right] \left\lvert \mathrm{grad} \left( \frac{\ell_\mathrm{T} \left[ 1 - \mathrm{e}^{-\frac{Re_\mathrm{T}^*}{30}} \right]}{1 + 2.9 \sqrt{A_2}} \right) \right\rvert$ | $0.83 \left[ 1 - \frac{2}{3} \left( C_\phi^{\mathrm{SH1}} - 1 \right) \right] \left\lvert \mathrm{grad} \left( \frac{\ell_\mathrm{T} \left[ 1 - \mathrm{e}^{-\frac{Re_\mathrm{T}^*}{30}} \right]}{1 + 2 A_2^{0.8}} \right) \right\rvert$ | $0.90 \left[ 1 - \frac{2}{3} \left( C_\phi^{\mathrm{SH1}} - 1 \right) \right] \left\lvert \mathrm{grad} \left( \frac{\ell_\mathrm{T} [1 - \mathrm{e}^{-\frac{Re_\mathrm{T}^*}{30}}]}{1 + 8 A_2^{0.8}} \right) \right\rvert$ |

**Table 1** (continued)

| Eq. | Term | GLVY | GV | WNF–LSS |
|---|---|---|---|---|
| (7e) | $C_\phi^{(\text{SI2})}$ | 0.002 | 0 | 0 |
| (7e) | $C_\phi^{(\text{SI3})}$ | $0.14\sqrt{\frac{\partial \ell_{\text{T}}^*}{\partial x_\ell}\frac{\partial \ell_{\text{T}}^*}{\partial x_\ell}}$ | 0 | 0 |

Notice that there is a typographic error in [35, (22), p. 1836], the turbulent Reynolds-number in the definition of $C_\phi^{(\text{RI})}$ and $C_\phi^{(\text{SI1})}$ for the GV RSM being $Re_{\text{T}}^*$ as above. The expression of $C_\phi^{(\text{RH})}$ for the GLVY and GV RSMs above (which does not use if-constructs [1, pp. 262–264]) is equivalent to

$$\left[C_\phi^{(\text{RH})}\right]_{\text{GLVY}} = \left[C_\phi^{(\text{RH})}\right]_{\text{GV}} = \left(1 - \max\left(0, 1 - \tfrac{1}{50} Re_{\text{T}}\right)\right) \times \begin{cases} 0.75\sqrt{A} & 0 \leq A < 0.55 \\ (0.75{+}1.3(A - 0.55))\, A^{0.5-1.3(A-0.55)} & 0.55 \leq A < 0.55 + \frac{0.25}{1.3} \\ A^{\frac{1}{4}} & 0.55 + \frac{0.25}{1.3} \leq A \leq 1 \end{cases}$$

Notice that there is a typographic error of the above expression of $\left[C_\phi^{(\text{RH})}\right]_{\text{GLVY}} = \left[C_\phi^{(\text{RH})}\right]_{\text{GV}}$ for $0.55 \leq A < 0.55 + \frac{0.25}{1.3}$ in [29, (22), p. 419, missing parentheses] and in [26, Table 1, p. 1370, misplaced parenthesis]

A general tensorial representation of the pressure terms $\Pi_{ij}$, which describes, by appropriate choice of the coefficients, all 3 models (Table 1), reads [28, (4–6), pp. 2851–2854]

$$\Pi_{ij} = \underbrace{\overbrace{\phi_{ij}^{(\mathrm{RH})} + \phi_{ij}^{(\mathrm{RI})}}^{\phi_{ij}^{(\mathrm{R})}} + \overbrace{\phi_{ij}^{(\mathrm{SH})} + \phi_{ij}^{(\mathrm{SI})}}^{\phi_{ij}^{(\mathrm{S})}}}_{\phi_{ij}} + \tfrac{2}{3}\phi_p\delta_{ij} + d_{ij}^{(p)} \tag{7a}$$

$$\begin{aligned} d_{ij}^{(p)} &= C^{(\mathrm{S}p1)}\bar{\rho}\frac{\mathrm{k}^3}{\varepsilon^3}\frac{\partial\varepsilon^*}{\partial x_i}\frac{\partial\varepsilon^*}{\partial x_j} + \frac{\partial}{\partial x_\ell}\left[C^{(\mathrm{S}p2)}(\overline{\rho u''_m u''_m u''_j}\delta_{i\ell} + \overline{\rho u''_m u''_m u''_i}\delta_{j\ell})\right] \\ &+ C^{(\mathrm{R}p)}\bar{\rho}\frac{\mathrm{k}^2}{\varepsilon^2}\breve{S}_{k\ell}a_{\ell k}\frac{\partial \mathrm{k}}{\partial x_i}\frac{\partial \mathrm{k}}{\partial x_j} \end{aligned} \tag{7b}$$

$$\begin{aligned} \phi_{ij}^{(\mathrm{R})} &= \underbrace{-C_\phi^{(\mathrm{RH})}\left(P_{ij} - \tfrac{1}{3}\delta_{ij}P_{mm}\right)}_{\phi_{ij}^{(\mathrm{RH})}} \\ &\quad \underbrace{+C_\phi^{(\mathrm{RI})}\left[\phi_{nm}^{(\mathrm{RH})}e_{\mathrm{I}_n}e_{\mathrm{I}_m}\delta_{ij} - \frac{3}{2}\phi_{in}^{(\mathrm{RH})}e_{\mathrm{I}_n}e_{\mathrm{I}_j} - \frac{3}{2}\phi_{jn}^{(\mathrm{RH})}e_{\mathrm{I}_n}e_{\mathrm{I}_i}\right]}_{\phi_{ij}^{(\mathrm{RI})}} \end{aligned} \tag{7c}$$

$$\begin{aligned} \phi_{ij}^{(\mathrm{S})} &= \underbrace{-C_\phi^{(\mathrm{SH1})}\bar{\rho}\varepsilon_{\mathrm{V}}a_{ij}}_{\phi_{ij}^{(\mathrm{SH1})}} \underbrace{+C_\phi^{(\mathrm{SI1})}\frac{\varepsilon_{\mathrm{V}}}{\mathrm{k}}\left[\bar{\rho}r_{nm}e_{\mathrm{I}_n}e_{\mathrm{I}_m}\delta_{ij} - \tfrac{3}{2}\bar{\rho}r_{ni}e_{\mathrm{I}_n}e_{\mathrm{I}_j} - \tfrac{3}{2}\bar{\rho}r_{nj}e_{\mathrm{I}_n}e_{\mathrm{I}_i}\right]}_{\phi_{ij}^{(\mathrm{SI1})}} \\ &\quad \underbrace{-C_\phi^{(\mathrm{SI2})}\bar{\rho}\frac{\mathrm{k}}{\varepsilon}\frac{\partial \mathrm{k}}{\partial x_\ell}\left[a_{ik}\frac{\partial r_{kj}}{\partial x_\ell} + a_{jk}\frac{\partial r_{ki}}{\partial x_\ell} - \tfrac{2}{3}\delta_{ij}a_{mk}\frac{\partial r_{km}}{\partial x_\ell}\right]}_{\phi_{ij}^{(\mathrm{SI2})}} \\ &\quad \underbrace{+C_\phi^{(\mathrm{SI3})}\left[\phi_{nm}^{(\mathrm{SI2})}e_{\mathrm{I}_n}e_{\mathrm{I}_m}\delta_{ij} - \tfrac{3}{2}\phi_{in}^{(\mathrm{SI2})}e_{\mathrm{I}_n}e_{\mathrm{I}_j} - \tfrac{3}{2}\phi_{jn}^{(\mathrm{SI2})}e_{\mathrm{I}_n}e_{\mathrm{I}_i}\right]}_{\phi_{ij}^{(\mathrm{SI3})}} \end{aligned} \tag{7d}$$

$$e_{\mathrm{I}_i} := \frac{\dfrac{\partial}{\partial x_i}\left(\dfrac{\ell_{\mathrm{T}}[1 - \mathrm{e}^{-\frac{Re_{\mathrm{T}}^*}{30}}]}{1 + 2\sqrt{A_2} + 2A^{16}}\right)}{\sqrt{\dfrac{\partial}{\partial x_\ell}\left(\dfrac{\ell_{\mathrm{T}}[1 - \mathrm{e}^{-\frac{Re_{\mathrm{T}}^*}{30}}]}{1 + 2\sqrt{A_2} + 2A^{16}}\right)\dfrac{\partial}{\partial x_\ell}\left(\dfrac{\ell_{\mathrm{T}}[1 - \mathrm{e}^{-\frac{Re_{\mathrm{T}}^*}{30}}]}{1 + 2\sqrt{A_2} + 2A^{16}}\right)}} \tag{7e}$$

where $\phi_{ij}$ denotes the redistribution tensor, $d_{ij}^{(p)}$ denotes pressure diffusion, the superscripts S and R denote slow and rapid terms [45], the superscripts H and I denote homogeneous and inhomogeneous terms [32], and the unit-vector $\mathbf{e}_{\mathrm{I}}$ was modelled [35] to point in the main direction of turbulence-inhomogeneity [29]. Notice that, although initially $\mathbf{e}_{\mathrm{I}}$ was designed to mimic the wall-normal direction in wall-echo terms [35], it turns out that inhomogeneous terms are also active at the shear-layer edge and in regions of recirculating flow [29], away from or even in absence of solid walls. As a consequence, the closure (7) must be considered as a whole, and inhomogeneous terms should be kept when computing free shear flows. Very near the walls, $\Pi_{ij} \to 0 \overset{(7a)}{\Longrightarrow} \phi_{ij} + \frac{2}{3}\phi_p\delta_{ij} \to -d_{ij}^{(p)}$, so that all authors [28] avoid the complexity of including terms in the model that would correctly mimic the individual behaviour of $\phi_{ij}$ and $d_{ij}^{(p)}$ as wall-distance $n \to 0$, which would cancel one another in Eq. 7a, but rather model $\Pi_{ij}$ as a whole in that region [28, Fig. 6, pp. 2855–2856], in line with the suggestion of Mansour et al. [57]. For this reason, the wall-echo-like [42] tensorial form of the terms containing $\mathbf{e}_{\mathrm{I}}$ in Eq. 7 is justified, because it was recently shown [32], from the analysis of DNS data, that it is in agreement with the near-wall behaviour of $\Pi_{ij}$ [32, Fig. 13 p. 41], unlike that of $\phi_{ij}$ [32, Fig. 12 p. 39]. The coefficients in Eqs. 5–7 are generally functions of the local turbulence state $(A, A_2, Re_{\mathrm{T}}, \cdots)$ and of its gradients, and depend on the particular RSM (Table 1).

The WNF–LSS [29] is a wall-normal-free extension of the Launder-Shima [52] RSM, which, in complex flows, performs better than the original wall-topology-dependent model, mainly because of the action of the inhomogeneous terms away from solid walls. The main drawback of this model is that, although it quite naturally improves upon 2-equation closures, it still underestimates separation [26]. The GV [35] RSM was developed to overcome this limitation, mainly by an optimized $C_{\phi}^{(\mathrm{RH})}$ coefficient (Table 1) of the isotropisation-of-production [42, 45, 52] closure of the rapid homogeneous part of redistribution (7d). The resulting model successfully predicted flows with large separation, but reattachment and especially relaxation were slightly slower than experimental data [66, 77]. The GLVY [28] RSM improves this behaviour [28, Fig. 9, p. 2858] through extended modelling of the inhomogeneous part of the slow redistribution terms $\phi_{ij}^{(\mathrm{SI})}$ (7a–7e) and of pressure diffusion $d_{ij}^{(p)}$ (7b), while using the same optimized closure for $\phi_{ij}^{(\mathrm{RH})}$ as the GV [35] RSM. It was also observed that the inclusion of these modifications influences the apparent transition behaviour [64] of the models, at low external turbulence conditions.

Comparing the 3 RSMs (Table 1), the WNF–LSS [29] RSM conceptually [45] includes pressure-diffusion in the Daly-Harlow [17] closure for $d_{ij}^{(u)}$, while the GV [35] RSM neglects $d_{ij}^{(p)}$; they both (WNF–LSS and GV) include the dissipation-rate anisotropy $\varepsilon_{ij} - \frac{2}{3}\varepsilon\delta_{ij}$ in the closure for $\phi_{ij}^{(\mathrm{S})}$ [52, 55]. On the contrary, the GLVY [28] RSM explicitly models both $d_{ij}^{(p)}$ and $\varepsilon_{ij} - \frac{2}{3}\varepsilon\delta_{ij}$.

Computations were also compared with the baseline linear Launder-Sharma [51] k-$\varepsilon$ closure, as implemented in [34].

### 2.2 Flow solver

Computations were performed using a structured multiblock solver [36], with WENO3 [49] reconstruction of the primitive variables, both mean-flow and turbulent, an $\mathrm{HLLC_h}$ approximate Riemann solver [6], and implicit multigrid dual-time-stepping pseudo-time-marching integration [37]. With the implicit implementation used [37] RSM computations are roughly $\sim$ 30 % more expensive compared to k-$\varepsilon$ calculations [14]. All of the computations presented in the paper were run using $L_{\mathrm{GRD}} = 3$ levels of multigrid with a V(2,0) sawtooth cycle [37] and dual-time-stepping parameters [36] $[\mathrm{CFL}, \mathrm{CFL}^*; M_{\mathrm{it}}, r_{\mathrm{TRG}}] = [100, 10; —, -1]$ (where CFL is the CFL-number for the pseudo-time-step, $\mathrm{CFL}^*$ is the

CFL-number for the dual pseudo-time-step, $M_{\mathrm{it}}$ is the number of dual subiterations, and $r_{\mathrm{TRG}} < 0$ is the target-reduction in orders-of-magnitude of the nonlinear pseudo-time-evolution system solution). This methodology is implemented in the open source software `aerodynamics` [2] with which the present results were obtained.

In all instances, a subsonic reservoir condition was applied at inflow [34, (24), p. 1324], a subsonic pressure condition [34, (26), p. 1324] was applied at outflow (uniform static pressure at outflow), and the no-slip walls were considered adiabatic [34, (25), p. 1324]. The inflow boundary condition was implemented using the method of finite waves [5]. Note that in this approach, the inflow boundary-layers are prescribed through the initial total pressure and total temperature profiles [30], but the streamwise mean-flow velocity $\tilde{u}$ at inflow is also influenced by the outgoing pressure-wave [10], and may therefore evolve differently for different turbulence closures [6, (Fig. 6), p. 209].

## 3 Assessment

The predictive capability of the 4 turbulence models (Section 2.1) was assessed by systematic comparison with experimental data for 3 duct-flow configurations [19, 39, 80]. Hereafter, the abbreviations GLVY RSM [28], GV RSM [35], WNF–LSS RSM [29] and LS k–$\varepsilon$ [51], are used consistently to denote each model.

### 3.1 Developing turbulent flow in a square duct [39]

The experimental data described by Gessner and Emery [39] were obtained [39, 41, 61] in a duct of square cross-section (Figs. 1, 2). The duct's height, which at incompressible flow conditions is also the duct's hydraulic diameter [81, (3.55), p. 123], is $D_{\mathrm{h}} = 2\mathrm{a} = 0.254$ m, and the length of the straight working section is $87D_{\mathrm{h}}$ [41, Fig. 2, p. 121]. The flow [39] is essentially incompressible (centerline Mach number $\bar{M}_{\mathrm{CL}} \approxeq 0.05$) at bulk Reynolds number $Re_{\mathrm{B}} \approxeq 250000$ ($Re_{\mathrm{B}} = \bar{u}_{\mathrm{B}} D_{\mathrm{h}} \nu^{-1}$, where $\bar{u}_{\mathrm{B}}$ is the bulk velocity and $\nu$ is the practically constant kinematic viscosity). The flow at the duct's inlet is nearly uniform, with very thin boundary-layers, whose virtual origin was estimated experimentally at $x \approxeq -0.65D_{\mathrm{h}}$ [41, p. 122]. These very thin boundary-layers grow until they fill the entire duct at $x \approxeq 32D_{\mathrm{h}}$ [41, p. 123] and interact to reach practically fully developed flow conditions at the last measurement station located at $x = 84D_{\mathrm{h}}$, near the exit of the duct's working section [41, Fig. 2, p. 121]. Measurements [39, 41, 61], taken at 5 axial planes (Fig. 3), include mean-flow $x$-wise velocities (Kiel probes in conjunction with wall static pressure taps), and secondary mean-flow velocities and Reynolds-stresses (hot-wire). They also include the detailed $x$-wise evolution of the centerline velocity (Kiel probe) and limited skin-friction data (Preston tubes) only at the last measurement station ($x = 84D_{\mathrm{h}}$) where the flow is considered fully developed [39, Fig. 2, p. 448].

In the Gessner and Emery [39] square duct, the main mechanisms are the interaction of stress-induced secondary flows, typical of the square cross-section [40], with boundary-layer entrainment [50]. The streamwise thickening of the wall-layers induces blockage, resulting in flow acceleration, which overshoots before stabilizing at the streamwise-invariant fully developed level (Fig. 2). Sufficient grid resolution is therefore required, both near the walls and at the centerline, to correctly reproduce the development and interaction of the boundary-layers, and as a consequence to obtain grid-convergence of the streamwise evolution of centerline velocity (Fig. 2). Results are presented for an $18 \times 10^6$ points grid

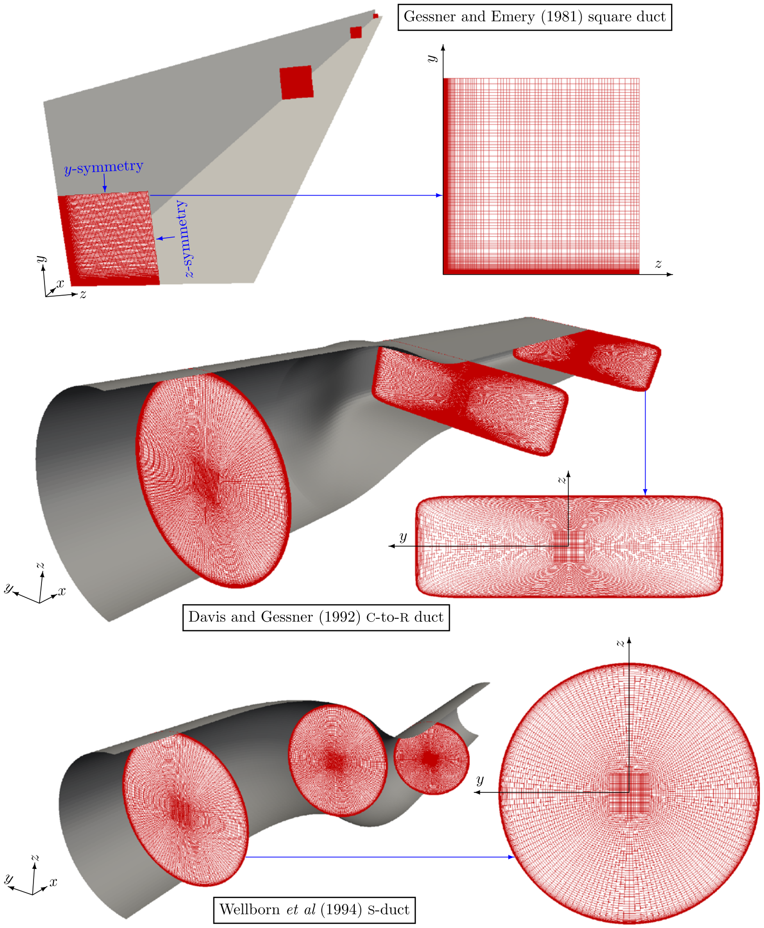

**Fig. 1** Computational grid topology (Table 2) for the square duct [39], the C-to-R transition duct [19] and the S-duct [80] test-cases (in all cases the $i$ = const grid-surfaces are $\perp$ $x$ planes)

(Table 2) discretizing one quadrant of the duct, with symmetry-conditions at the $y$- and $z$-wise symmetry-planes. The computational domain $L_x \times L_y \times L_z = 98.43 D_\mathrm{h} \times \frac{1}{2} D_\mathrm{h} \times \frac{1}{2} D_\mathrm{h}$ was slightly longer ($0 \leq x \leq 25$ m $\approxeq 98 D_\mathrm{h} > 87 D_\mathrm{h}$) than the actual duct [41] to avoid interaction between the uniform outflow pressure boundary-condition and computed results at the last measurement station ($x = 84 D_\mathrm{h}$). The grid (Fig. 1) is uniform in the streamwise ($x$) direction, while in the $y$ and $z$ directions, 65 % of the $N_j = N_k = 149$ points are stretched geometrically near the walls [31] with ratio $r_j = r_k = 1.067$ (Table 2), the remaining 35 % being uniformly distributed in the centerline region. For the investigated flow conditions, the first node at the walls is located at $\Delta y_w^+ = \Delta z_w^+ \lessapprox \frac{1}{2}$ (Table 2).

At inflow (Table 3), standard atmospheric total conditions ($p_{t_{\mathrm{CL_i}}} = 101325$ Pa, $T_{t_{\mathrm{CL_i}}} = 288$ K), with a turbulent intensity $T_{u_{\mathrm{CL_i}}} = 1$ % and turbulent lengthscale $\ell_{\mathrm{T_{CL_i}}} = 50$ mm, were assumed at the centerline. The outflow pressure was adjusted to obtain the correct

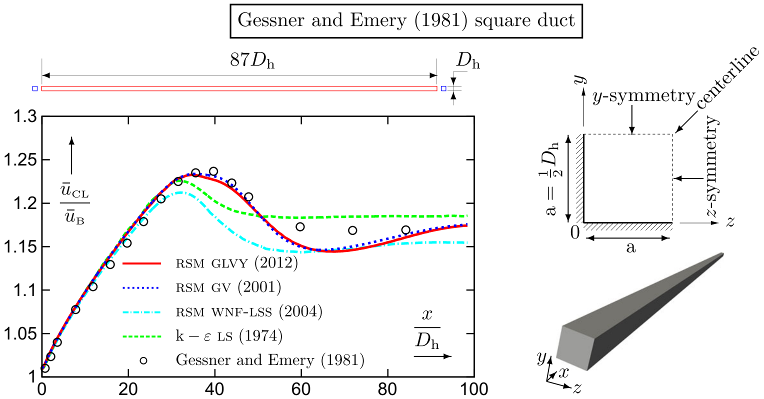

**Fig. 2** Comparison of measured [39] streamwise evolution of $x$-wise centerline ($y = z =$ a) velocity $\bar{u}_{CL}$ with computations ($18 \times 10^6$ points grid discretizing $\frac{1}{4}$ of the square duct; Table 2) using (Section 2.1) the GV [35], the WNF–LSS [29] and the GLVY [28] RSMs, and the LS [51] linear k–$\varepsilon$ model, for developing turbulent flow in a square duct ($Re_B = 250000$, $\bar{M}_{CL} \approxeq 0.05$; Table 3)

$Re_B = 250000$ ($p_o = 0.995 p_{t_{CL_i}}$) corresponding to an inlet Mach number at centerline $M_{CL_i} \approxeq 0.0516$ (Table 3). The initial inflow boundary-layer was adjusted to a different value for each turbulence model (0.1 mm $\leq \delta_i \leq$ 0.875 mm) to obtain a close fit to the experimental centerline velocity $\bar{u}_{CL}$ in the entry region of the duct ($x \in [0, 10D_h]$; Fig. 2). Another approach would have been to start the computations with 0 initial inflow boundary-layer thickness and to adjust in the post-processing phase the virtual origin of the developing boundary-layers ($x$-shift the results) to best fit the experimental centerline velocity $\bar{u}_{CL}$ in the entry region.

The computations using the 3 RSMs and the k–$\varepsilon$ model (Section 2.1) highlight (Figs. 2–7) the great sensitivity of the predictions to the turbulence model. It should be stated from the outset that the underlying Boussinesq hypothesis [82, pp. 273–278] renders the linear LS k–$\varepsilon$ model ill-adapted for the present Reynolds-stress-anisotropy-driven flow [39]; results with the baseline LS k–$\varepsilon$ model are only included as a reference to the limitations of standard Boussinesq models.

In the initial part of the duct ($0 \lessapprox x \lessapprox 30D_h$; Fig. 2), all of the 4 models (Section 2.1) correctly predict the thickening of and associated blockage by the developing wall-layers, which determine, because of massflow conservation, the centerline velocity $\bar{u}_{CL}$. Recall that the initial conditions for the boundary-layers at inflow ($x = 0$) were independently adjusted for each turbulence model (Table 3), precisely to obtain the best fit of $\bar{u}_{CL}$ in this region ($0 \lessapprox x \lessapprox 30D_h$; Fig. 2). The best prediction is obtained by the GLVY and GV RSMs (whose results are quite similar; Fig. 2), both of which correctly simulate the $\bar{u}_{CL}$-peak ($30D_h \lessapprox x \lessapprox 50D_h$; Fig. 2) and the final fully developed level at $x = 84D_h$ (Fig. 2). However, the results of the GLVY and GV RSMs do not tend to this final level monotonically, as the experimental data in the region $50D_h \lessapprox x \lessapprox 80D_h$ seem to indicate, but exhibit a ∼2.5 % undershoot before reaching the correct fully developed level at $x = 84D_h$ (Fig. 2). In contrast with the GLVY and GV RSMs, the WNF–LSS RSM severely underpredicts the experimentally observed $\bar{u}_{CL}$-peak ($30D_h \lessapprox x \lessapprox 60D_h$; Fig. 2) and also underpredicts by ∼2.5 % the final fully developed value ($x = 84D_h$; Fig. 2). On the other hand, the WNF–

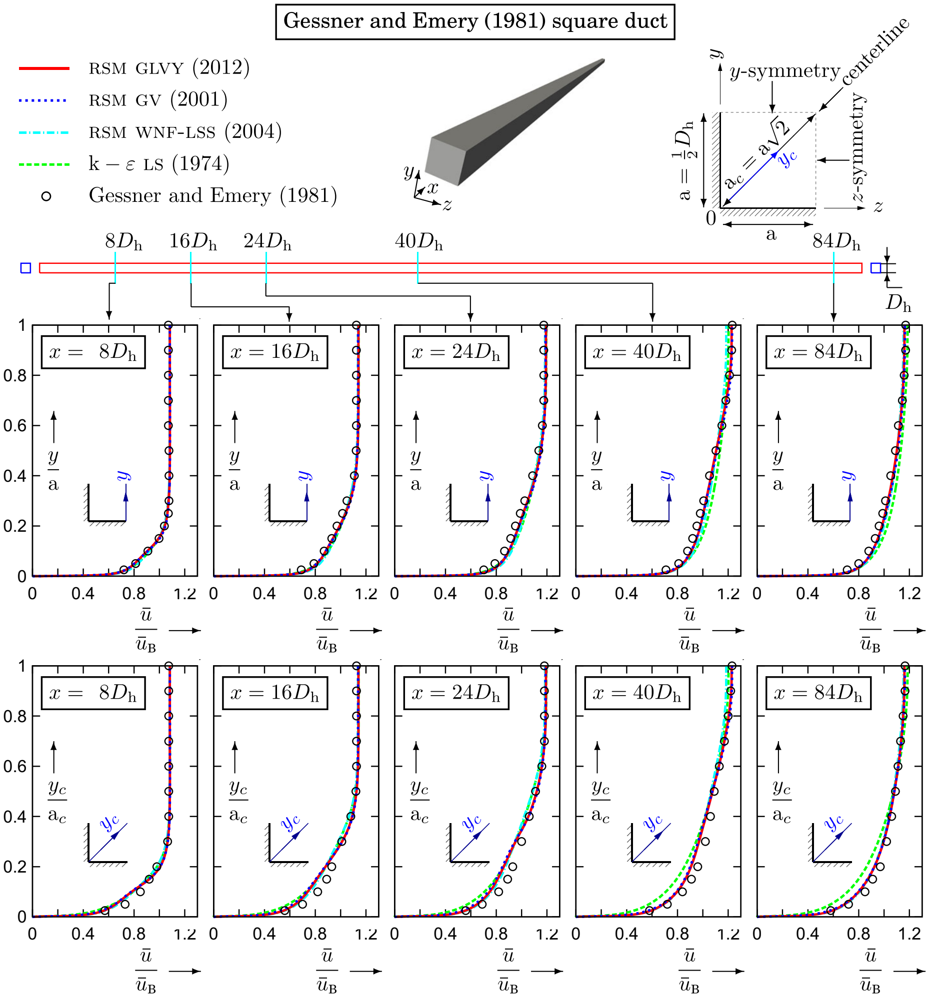

**Fig. 3** Comparison of measured [39] streamwise ($x$-wise) velocity $\bar{u}$, along the wall-bisector ($z$ = a) and along the corner-bisector ($z = y$), at the 5 experimental measurement stations, with computations ($18 \times 10^6$ points grid discretizing $\frac{1}{4}$ of the square duct; Table 2) using (Section 2.1) the GV [35], the WNF–LSS [29] and the GLVY [28] RSMs, and the LS [51] linear k–$\varepsilon$ model, for developing turbulent flow in a square duct ($Re_B = 250000$, $\bar{M}_{CL} \approxeq 0.05$; Table 3)

LSS RSM tends to this final value in a less oscillatory fashion ($40D_h \lessapprox x \lessapprox 80D_h$; Fig. 2). Finally, the LS k–$\varepsilon$ model also underestimates the $\bar{u}_{CL}$-peak ($30D_h \lessapprox x \lessapprox 60D_h$; Fig. 2) and tends monotonically to an ~1.5 % overestimated value of the final fully developed level ($x = 84D_h$; Fig. 2).

The detailed evolution of the streamwise mean-flow velocity $\bar{u}$ profiles (Fig. 3) provides insight into the predictions of centerline velocity $\bar{u}_{CL}$ (Fig. 2) by the different models. The term wall-bisector was used by Gessner and Emery [39] to denote the symmetry-plane at $z = \mathrm{a} = \frac{1}{2}D_h$ and the term corner-bisector to denote the diagonal with distance $y_c := \frac{\sqrt{2}}{2}(y - y_w) + \frac{\sqrt{2}}{2}(z - z_w)$ from the corner (notice that $\mathrm{a}_c^{-1} y_c = \mathrm{a}^{-1} y = \mathrm{a}^{-1} z$ along the

**Table 2** Computational grids and mesh-generation parameters [31, 33] for the square duct [39], the C-to-R transition duct [19] and the S-duct [80] test-cases

| Configuration | Grids | | | | | | | | | |
|---|---|---|---|---|---|---|---|---|---|---|
| | $N_p$ | $n_D$ | Type | $N_i \times N_j \times N_k$ | $N_{j_s}$ | $r_j$ | $N_{k_s}$ | $r_k$ | $r_\square$ | $\Delta n_w^+$ |
| Square duct | $17.8 \times 10^6$ | 1 | H | $801 \times 149 \times 149$ | 97 | 1.067 | 97 | 1.067 | – | $\sim 0.5$ |
| C-to-R duct | $9.4 \times 10^6$ | 1 | O□ | $209 \times 209 \times 201$ | – | – | 201 | 1.060 | 0.15 | $\sim 0.2$ |
| | | 2 | H□ | $209 \times 53 \times 53$ | – | – | – | – | – | – |
| S-duct | $1.9 \times 10^6$ | 1 | O□ | $161 \times 129 \times 81$ | – | – | 81 | 1.220 | 0.15 | $\sim 0.4$ |
| | | 2 | H□ | $161 \times 33 \times 33$ | – | – | – | – | – | – |

$N_p$: number of grid-points; $n_D$: domain index; type: domain grid-type; H:H-type grid ($x \times y \times z$); O□: circumferentially O-type grid ($x \times \ -\theta \times R$) between the duct-casing and the inner square domain ($n_D = 2$) around the centerline; H□: H-type grid for the inner square domain ($n_D = 2$) around the centerline; $N_i \times N_j \times N_k$: grid-points; $N_{j_s}$, $N_{k_s}$: number of points geometrically stretched near the solid walls; $r_j$, $r_k$: geometric progression ratio; $r_\square$: ratio of the side of the square domain around the centerline to the size of the cross-section (defined as the average of its projections on the $y$ and $z$ axes); $\Delta n_w^+$ nondimensional wall-normal size of the first grid-cell in wall-units [31]

**Table 3** Initial (ICs) and boundary-conditions (BCs) for the square duct [39], the C-to-R transition duct [19] and the S-duct [80] test-cases, using the GLVY RSM [28], the GV RSM [35], the WNF–LSS RSM [29] and the LS k-$\varepsilon$ [51]

| Configuration | Model | ICs and BCs | | | | | | | | |
|---|---|---|---|---|---|---|---|---|---|---|
| | | $\delta_\mathrm{i}$ (mm) | $\Pi_{\mathrm{C_i}}$ | $M_{\mathrm{CL_i}}$ | $T_{u_{\mathrm{CL_i}}}$ | $\ell_{\mathrm{T_{CL_i}}}$ (mm) | $p_{t_{\mathrm{CL_i}}}$ (Pa) | $T_{t_{\mathrm{CL_i}}}$ (K) | $q_w$ (W m$^{-2}$) | $p_\mathrm{o}$ (Pa) |
| Square duct | GLVY RSM | 0.875 | 0 | 0.0516 | 1 % | 50 | 101325 | 288 | 0 | $0.995 p_{t_{\mathrm{CL_i}}}$ |
| | GV RSM | 0.300 | | | | | | | | |
| | WNF–LSS RSM | 0.100 | | | | | | | | |
| | LS k–$\varepsilon$ | 0.100 | | | | | | | | |
| C-to-R duct | GLVY RSM | 30.85 | 0.50 | 0.0940 | 0.3 % | 50 | 101325 | 298.3 | 0 | 100627 |
| | GV RSM | 30.85 | | | | | | | | |
| | WNF–LSS RSM | 30.85 | | | | | | | | |
| | LS k–$\varepsilon$ | 28.00 | | | | | | | | |
| S-duct | GLVY RSM | 10.5 | 0.25 | 0.60 | 0.65 % | 50 | 111330 | 296.4 | 0 | 98600 |
| | GV RSM | 10.5 | 0.25 | | | | | | | 98600 |
| | WNF–LSS RSM | 10.3 | 0.35 | | | | | | | 98900 |
| | LS k–$\varepsilon$ | 10.8 | 0.40 | | | | | | | 98600 |

$\delta_\mathrm{i}$: boundary-layer thickness at inflow (IC); $\Pi_{\mathrm{C_i}}$: inflow boundary-layer Coles-parameter [30] (IC); $M_{\mathrm{CL_i}}$: inflow centerline Mach-number (IC); $T_{u_{\mathrm{CL_i}}}$: turbulent intensity outside of the boundary-layers at inflow [30]; $\ell_{\mathrm{T_{CL_i}}}$: turbulent lengthscale outside of the boundary-layers at inflow [30]; $p_{t_{\mathrm{CL_i}}}$: inflow centerline total pressure (BC); $T_{t_{\mathrm{CL_i}}}$: inflow centerline total temperature (BC); $q_w$: wall heat-flux (BC); $p_\mathrm{o}$: outflow static pressure (BC) diagonal whose length between the corner and the centerline is $\mathrm{a}_c := \mathrm{a}\sqrt{2}$). The flowfield along the corner-bisector $y_c$ is strongly influenced by the secondary flows. The GLVY and GV RMSs yield quite accurate results for the $\bar{u}$ profiles (Fig. 3), both along the wall-bisector $y$ ($z = \mathrm{a}$; Fig. 3) and along the corner-bisector $y_c$ ($z = y$; Fig. 3). Notice, nonetheless, that no experimental data are available in the region $50D_\mathrm{h} \lessapprox x \lessapprox 80D_\mathrm{h}$ where the slight undershoot in centerline velocity $\bar{u}_\mathrm{CL}$ was observed (Fig. 2). The predictions of the WNF–LSS RSM for the streamwise velocity $\bar{u}$ (Fig. 2) are similar to those of the GLVY and GV RSMs, except for the outer part (wake region) of the boundary-layer, especially at $x = 40D_\mathrm{h}$ along the wall-bisector $y$ ($z = \mathrm{a}$; Fig. 3) and at $x \in \{8D_\mathrm{h}, 16D_\mathrm{h}, 24D_\mathrm{h}, 40D_\mathrm{h}\}$ along the corner-bisector $y_c$ ($z = y$; Fig. 3). Finally, expectedly, the linear LS k–$\varepsilon$ model makes the worst prediction, especially at the last 2 stations $x \in \{40D_\mathrm{h}, 84D_\mathrm{h}\}$, where it overpredicts $\bar{u}$ in the lower part of the boundary-layer along the wall-bisector $y$ ($z = \mathrm{a}$; Fig. 3) and rather severely underpredicts it in the lower part of the boundary-layer along the corner-bisector $y_c$ ($z = y$; Fig. 3).

By the continuity equation the $x$-wise development of the streamwise velocity $\bar{u}$ is related to the profiles of the in-plane velocity components, $\bar{v}$ and $\bar{w}$. Measurements of the $y$-wise component $\bar{v}$ are only available at the last 2 measurement planes ($x \in \{40D_\mathrm{h}, 84D_\mathrm{h}\}$; Fig. 4). Notice first that, along the wall-bisector $y$ ($z = \mathrm{a}$) we have $\bar{w} = 0$ by symmetry, while along the corner-bisector $y_c$ ($z = y$) we have $\bar{w} = \bar{v}$ again by symmetry. Contrary to the results for the profiles of streamwise velocity $\bar{u}$ (Fig. 3), the predictions of the $y$-wise component $\bar{v}$ have noticeable differences between the various models (Fig. 4). The GLVY RSM gives the best prediction of secondary velocities, both along the wall-bisector $y$ ($z = \mathrm{a}$; Fig. 4) and along the corner-bisector $y_c$ ($z = y$; Fig. 4). Although the agreement of the GLVY RSM results with measurements is quite satisfactory at $x = 40D_\mathrm{h}$, the secondary velocities are underestimated at the last measurement station $x = 84D_\mathrm{h}$ (Fig. 4). The GV RSM gives results very close to those of the GLVY RSM along the corner-bisector $y_c$ ($z = y$; Fig. 4), some discrepancies very near the corner ($y_c \lessapprox 0.1\mathrm{a}_c$; Fig. 4) notwithstanding, but underestimates $\bar{v}$ along the wall-bisector $y$ ($z = \mathrm{a}$; Fig. 4) at the outer part of the boundary-layer. The WNF–LSS RSM, does predict secondary flows, less intense than the GLVY and GV RSMs (Fig. 4), while the linear LS k–$\varepsilon$ model completely fails (Fig. 4), implying that the strong values of $\bar{v}$ at the last measurement stations ($x \in \{40D_\mathrm{h}, 84D_\mathrm{h}\}$; Fig. 4) are the consequence of secondary turbulence-driven flows, in a region where the flow approaches the fully developed state [8, 39, 40].

The comparison of computational results with measured Reynolds-stresses (Figs. 5–7) is consistent with the comparisons of the mean-flow velocity field (Figs. 3, 4). The GLVY and GV RSMs give the best overall prediction of the shear Reynolds-stresses, $\overline{u'v'}$ along the wall-bisector $y$ ($z = \mathrm{a}$; Fig. 5) and $\overline{u'v'} = \overline{u'w'}$ (by symmetry) along the corner-bisector $y_c$ ($z = y$; Fig. 5), but overestimate their magnitude, especially along the corner-bisector $y_c$ ($z = y$; Fig. 5). The experimental data are generally consistent with the symmetry condition $\overline{u'v'} = \overline{u'w'}$ along the corner-bisector $y_c$ ($z = y$; Fig. 5), except at $x = 40D_\mathrm{h}$ in the outer part of the boundary-layer ($y_c \gtrapprox 0.4\mathrm{a}_c$; $z = y$; Fig. 5). The overprediction of the shear Reynolds-stress $\overline{u'v'} = \overline{u'w'}$ along the corner-bisector $y_c$ at $x = 40D_\mathrm{h}$ ($z = y$; Fig. 5) is not consistent with the satisfactory prediction of the mean-flow velocity field at this station ($x = 40D_\mathrm{h}$; $z = y$; Figs. 3, 4), especially as the $x$-wise gradients predicted by the GLVY and GV RSMs are in good agreement with experimental data at $x = 40D_\mathrm{h}$ (Fig. 2). Regarding the last measurement station at $x = 84D_\mathrm{h}$, the shear Reynolds-stress $\overline{u'v'} = \overline{u'w'}$ predicted by the GLVY and GV RSMs along the corner-bisector $y_c$ ($x = 84D_\mathrm{h}$; $z = y$; Fig. 5) is closer to the experimental data than at $x = 40D_\mathrm{h}$, but computed values are still larger in

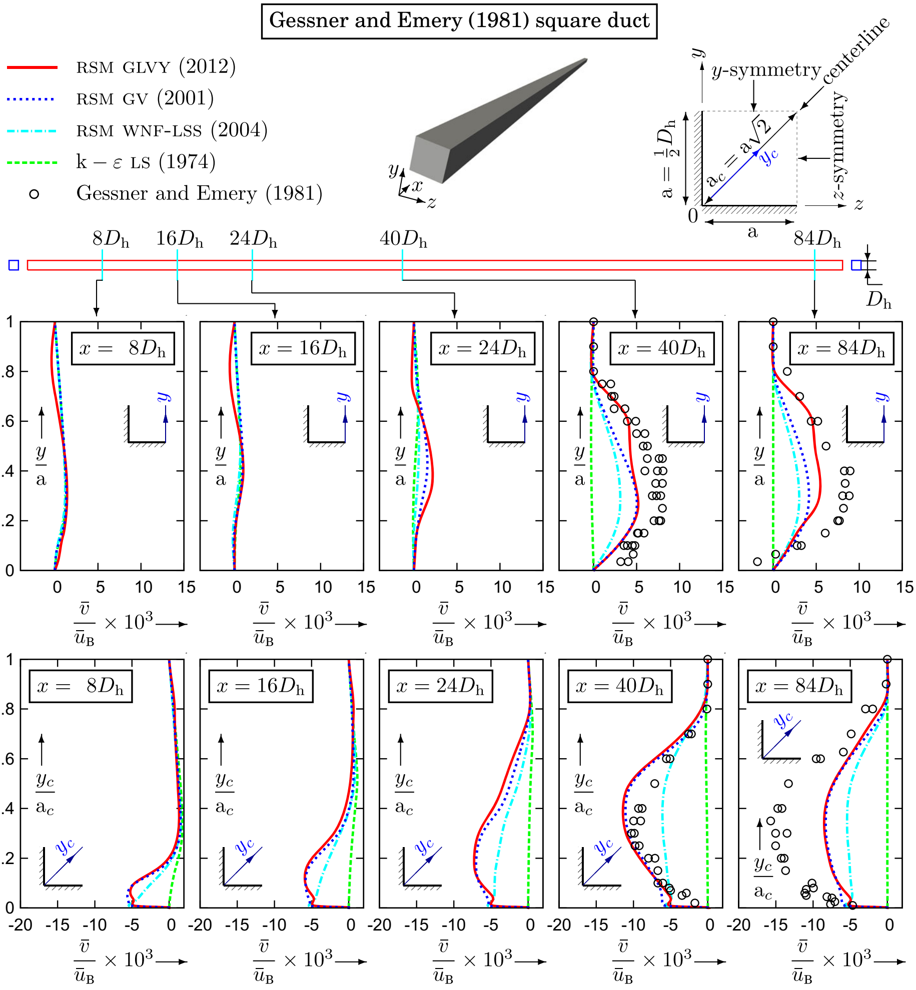

**Fig. 4** Comparison of measured [39] wall-normal ($y$-wise) velocity $\bar{v}$, along the wall-bisector ($z$ = a) and along the corner-bisector ($z = y$, where by symmetry $\bar{w} = \bar{v}$), at the 5 experimental measurement stations, with computations ($18 \times 10^6$ points grid discretizing $\frac{1}{4}$ of the square duct; Table 2) using (Section 2.1) the GV [35], the WNF–LSS [29] and the GLVY [28] RSMs, and the LS [51] linear k–$\varepsilon$ model, for developing turbulent flow in a square duct ($Re_B = 250000$, $\bar{M}_{CL} \approxeq 0.05$; Table 3)

magnitude by ∼30 %. The WNF–LSS RSM and LS k–$\varepsilon$ models predictions of the shear Reynolds-stress $\overline{u'v'}$ along the wall-bisector $y$ ($z$ = a; Fig. 5) are generally similar with those of the GLVY and GV RSMs, in satisfactory agreement with measurements. On the other hand, the WNF–LSS RSM and the LS k–$\varepsilon$ model perform less satisfactorily than the GLVY and GV RSMs regarding the prediction of the shear Reynolds-stresses $\overline{u'v'} = \overline{u'w'}$ (by symmetry) along the corner-bisector $y_c$ ($z = y$; Fig. 5), the WNF–LSS RSM, expectedly, performing better than the linear LS k–$\varepsilon$ model. The GLVY and GV RSMs predict quite accurately the streamwise normal Reynolds-stress $\overline{u'^2}$ (Fig. 6) both along the wall-bisector $y$ ($z$ = a) and the corner-bisector $y_c$ ($z = y$), some slight discrepancies along the corner-

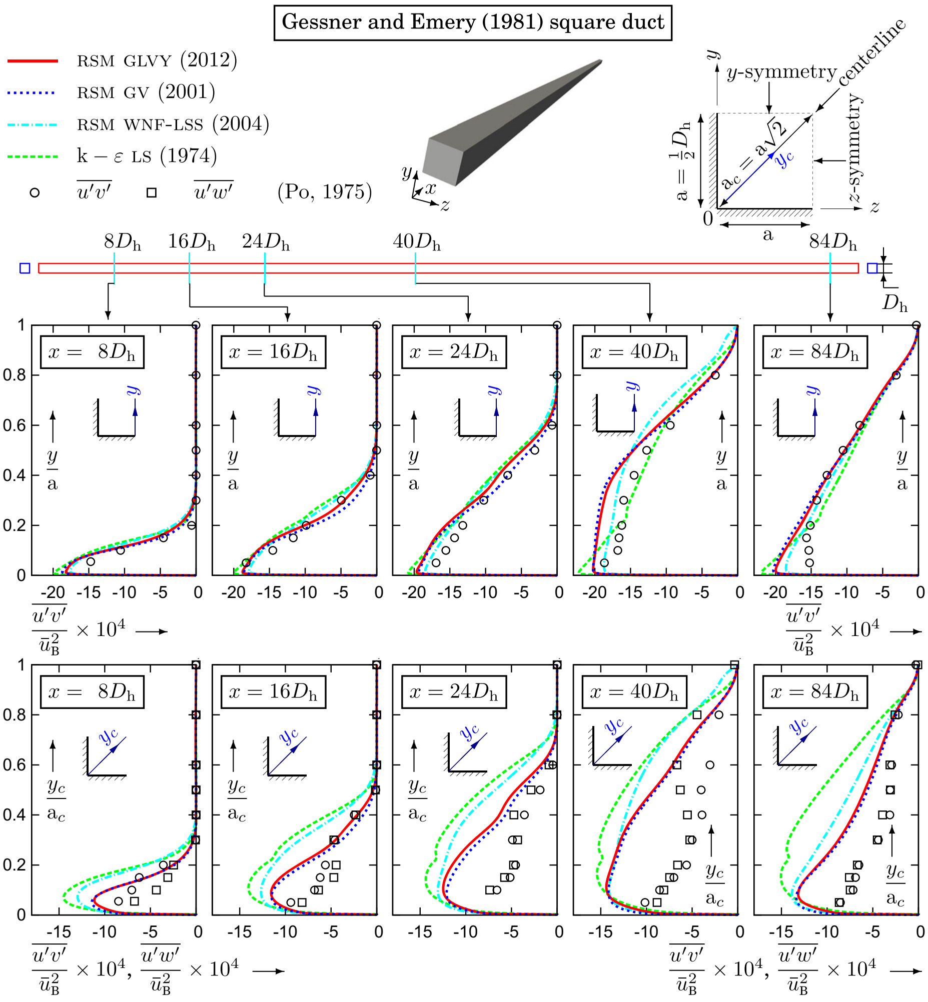

**Fig. 5** Comparison of measured [39] Reynolds shear-stresses, $\overline{u'v'}$ along the wall-bisector ($z = a$) and along the corner-bisector ($z = y$), and $\overline{u'w'}$ along the corner-bisector ($z = y$, where by symmetry $\overline{u'w'} = \overline{u'v'}$), at the 5 experimental measurement stations, with computations ($18 \times 10^6$ points grid discretizing $\frac{1}{4}$ of the square duct; Table 2) using (Section 2.1) the GV [35], the WNF–LSS [29] and the GLVY [28] RSMs, and the LS [51] linear k–ε model, for developing turbulent flow in a square duct ($Re_B = 250000$, $\bar{M}_{CL} \approxeq 0.05$; Table 3)

bisector $y_c$ ($x \in \{16D_h, 24D_h, 40D_h\}$; $z = y$; Fig. 6) notwithstanding. The predictions of the streamwise normal Reynolds-stress $\overline{u'^2}$ by the WNF–LSS RSM and the LS k–ε model are, again, less satisfactory (Fig. 6), especially along the wall-bisector $y$ ($z = a$; Fig. 6). Regarding the prediction of the other normal Reynolds-stresses, wall-normal $\overline{v'^2}$ along the wall-bisector $y$ ($z = a$), transverse $\overline{w'^2}$ along the wall-bisector $y$ ($z = a$), and secondary $\overline{v'^2} = \overline{w'^2}$ along the corner-bisector $y_c$ ($z = y$), all 3 RSMs (GLVY, GV and WNF–LSS) are in good agreement with experimental data (Fig. 7), in contrast with the linear LS k–ε model, which completely fails in predicting the Reynolds-stress tensor anisotropy (Fig. 7), because of the pathological shortcomings of the Boussinesq hypothesis [82, pp. 273–278].

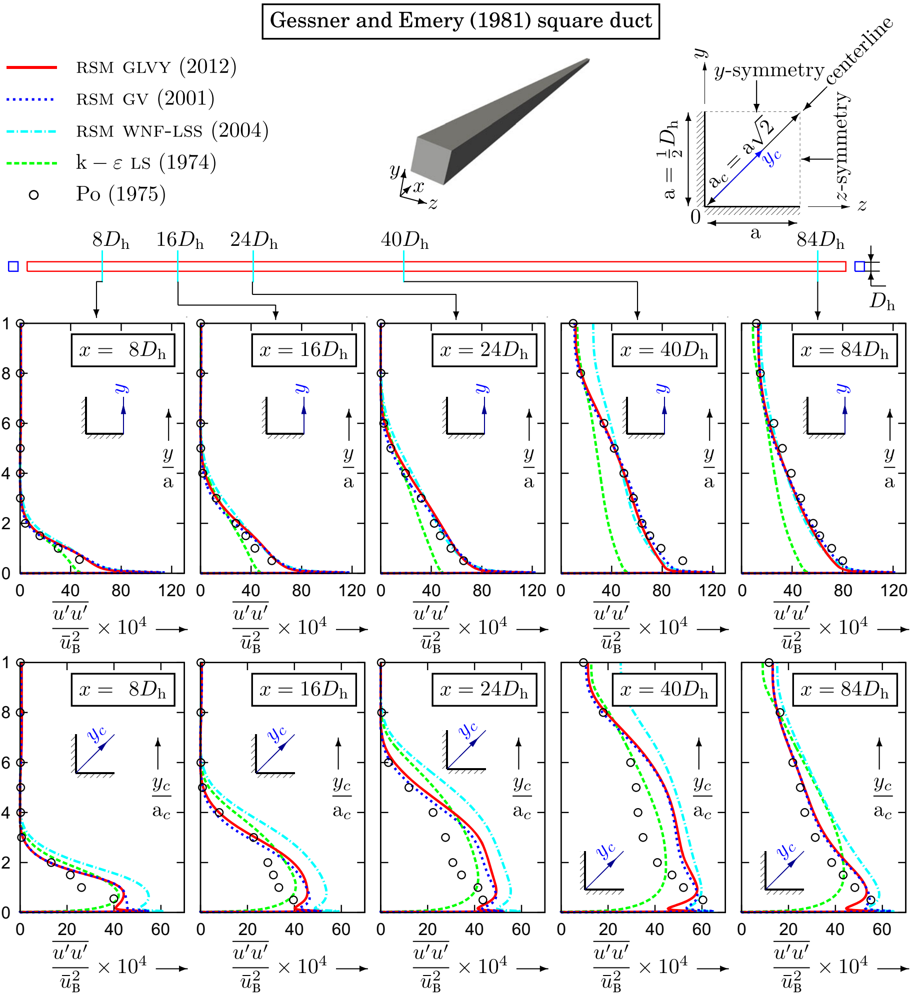

**Fig. 6** Comparison of measured [39] streamwise diagonal Reynolds-stress $\overline{u'u'}$, along the wall-bisector ($z = \mathrm{a}$) and along the corner-bisector ($z = y$), at the 5 experimental measurement stations, with computations ($18 \times 10^6$ points grid discretizing $\frac{1}{4}$ of the square duct; Table 2) using (Section 2.1) the GV [35], the WNF–LSS [29] and the GLVY [28] RSMs, and the LS [51] linear k–$\varepsilon$ model, for developing turbulent flow in a square duct ($Re_\mathrm{B} = 250000$, $\bar{M}_\mathrm{CL} \approxeq 0.05$; Table 3)

To explain the better agreement with experimental data of the GLVY and GV RSMs, compared to the WNF–LSS RSM (Figs. 2–7), it is interesting to examine the differences between the closures (Table 1). The differences (Table 1) between the GLVY and GV RSMs (pressure diffusion $d_{ij}^{(p)}$, explicit algebraic modelling for $\varepsilon_{ij}$, extra inhomogeneous terms in $\Pi_{ij}$) do not have any substantial influence on the prediction of the [39] square duct flow, the only noticeable difference being the better prediction by the GLVY RSM of the wall-normal velocity $\bar{v}$ along the wall-bisector $y$ ($x \in \{40D_\mathrm{h}, 84D_\mathrm{h}\}$; $z = \mathrm{a}$; Fig. 4), especially in the outer part of the boundary-layer ($y \gtrapprox 0.6\mathrm{a}$). There are 2 main differences between the WNF–LSS RSM and the GV RSM (Table 1), the coefficient-function $C_\phi^{(\mathrm{RH})}$ of the

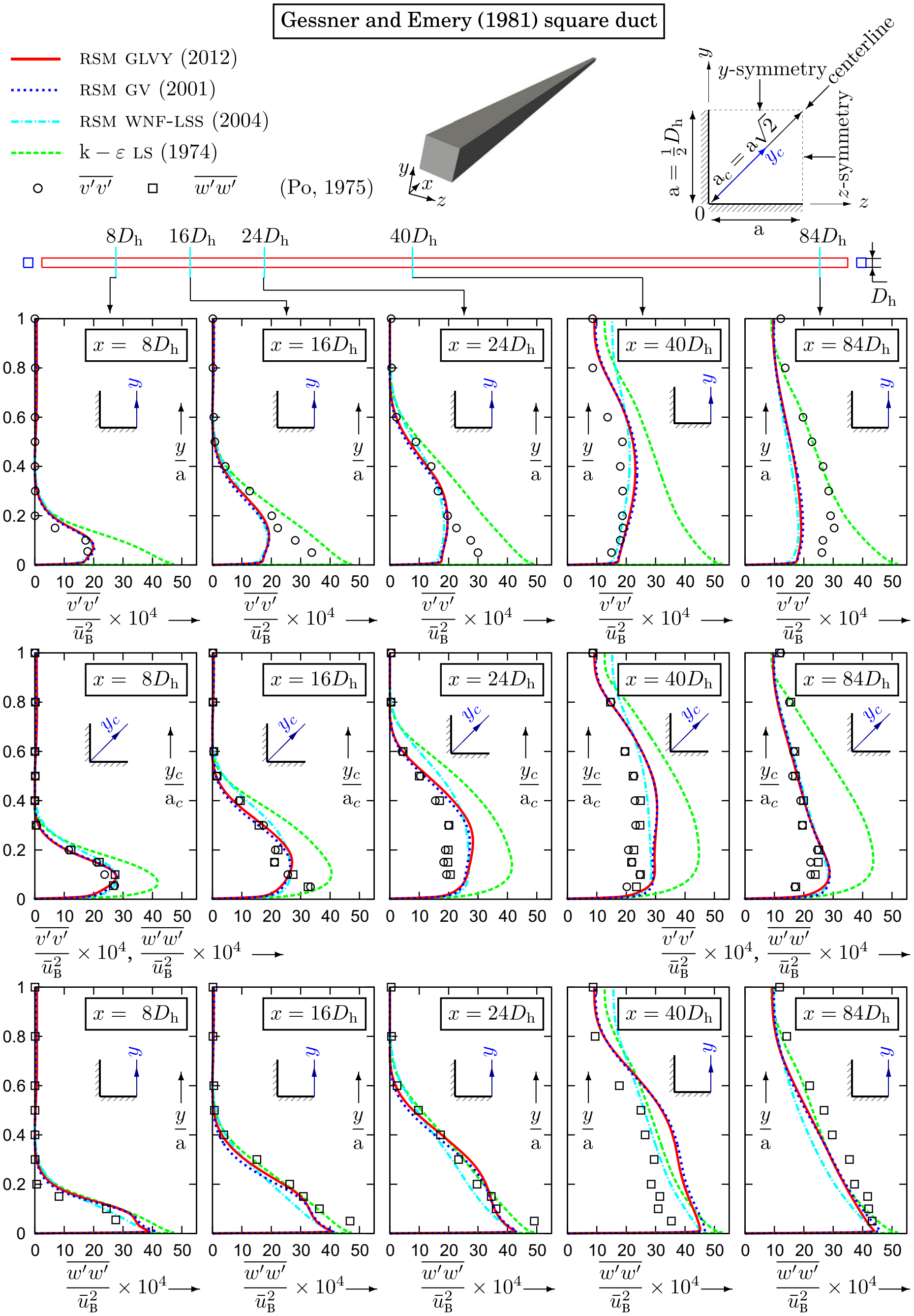

**Fig. 7** Comparison of measured [39] normal Reynolds-stresses $\overline{v'v'}$ and $\overline{w'w'}$, along the wall-bisector ($z=a$) and along the corner-bisector ($z=y$, where by symmetry $\overline{w'w'}=\overline{v'v'}$), at the 5 experimental measurement stations, with computations ($18\times10^6$ points grid discretizing $\frac{1}{4}$ of the square duct; Table 2) using (Section 2.1) the GV [35], the WNF–LSS [29] and the GLVY [28] RSMs, and the LS [51] linear k–$\varepsilon$ model, for developing turbulent flow in a square duct ($Re_B=250000$, $\bar{M}_{CL}\approxeq 0.05$; Table 3)

isotropisation-of-production model for the homogeneous rapid part of redistribution (7d), and the closure for the triple velocity correlations (5). The coefficient $C_\phi^{(\mathrm{RH})}$ (Table 1) in the GLVY and GV RSMs was designed [35, Fig. 4, p. 1838] to increase rapidly towards a value of 1 when Lumley's [55] flatness parameter $A$ (1b) increases beyond 0.55 (which is approximately the value of $A$ just before the beginning of the logarithmic zone of the flat-plate boundary-layer velocity profile). Regarding turbulent diffusion (Table 1), the GLVY and GV RSMs use the Hanjalić-Launder [46] closure, whereas the WNF–LSS RSM uses the Daly-Harlow [17] closure (Section 2.1). Obviously (Figs. 2–7), the combined use of these 2 modelling choices in the GLVY and GV RSMs substantially improves the prediction of the [39] square duct flow compared to the WNF–LSS RSM. To put into perspective the specific influence of each of the 2 mechanisms, a test-model (not recommended for practical use), hereafter GV–DH RSM, which combines the $C_\phi^{(\mathrm{RH})}$ coefficient-function of the GLVY and GV RSMs (Table 1) with the Daly-Harlow [17] closure for turbulent diffusion (with appropriate recalibration of various coefficients to get the correct log-law in flat-plate boundary-layer flow; [29, Table 2, p. 418]), has been developed [29, 77]. Calculations of the [39] square duct flow with the GV, GV–DH and WNF–LSS RSMs, using the same inflow boundary-layer-thickness [29, $\delta_{y_i} = \delta_{z_i} = 0.5$ mm, Fig. 7, p. 422] for all of the models, indicate that $C_\phi^{(\mathrm{RH})}$ influences the initial part of the region where the boundary-layers on the 4 walls first merge ($30D_\mathrm{h} \lessapprox x \lessapprox 40D_\mathrm{h}$; Fig. 2) whereas turbulent diffusion is active especially in the region after the centerline velocity peak ($40D_\mathrm{h} \lessapprox x \lessapprox 60D_\mathrm{h}$; Fig. 2).

### 3.2 Circular-to-rectangular transition duct [19]

This configuration [18, 19] is a transition duct where the cross-section changes (Fig. 1) from circular at the inlet to quasi-rectangular at the exit (rectangle aspect-ratio of 3 at the exit section). Such geometries are typical of the transition section necessary to connect an aircraft engine exit to a rectangular nozzle [62]. The precise geometrical specification of the duct's cross-section is superelliptical [18, (A.1), p. 136] so that the exit section has slightly rounded corners with a "*variable radius fillet*" [18, p. 2]. The diameter of the circular inlet section is $D_{\mathrm{CSG}_1} = 2R_{\mathrm{CSG}_1} = 0.2043$ m [18, p. 137], and the length of the transition section (from inlet station 2 to exit station 5; Fig. 8) is $\frac{3}{2}D_{\mathrm{CSG}_1}$. Although there is no net cross-sectional area change, between inflow and outflow, locally [54, Fig. 4, p. 242], the transition section is divergent [18, p. 2] from inlet to midpoint (cross-sectional area increase of 15 %) and then convergent from midpoint to exit (cross-sectional area decreases back to the inlet area). The duct is cylindrical upstream (circular cross-section of diameter $D_{\mathrm{CSG}_1}$ for several diameters upstream of station 2) and downstream (quasi-rectangular superelliptical constant cross-section for several inlet-diameters $D_{\mathrm{CSG}_1}$ downstream of station 5) of the transition section [18, Fig. 3.1, p. 22].

The flow [19] is essentially incompressible (centerline Mach number $\bar{M}_\mathrm{CL} \approxeq 0.10$) at bulk Reynolds number $Re_\mathrm{B} \approxeq 390000$ ($Re_\mathrm{B} = \bar{u}_\mathrm{B} D_{\mathrm{CSG}_1} \nu^{-1}$, where $\bar{u}_\mathrm{B}$ is the bulk velocity and $\nu$ is the practically constant kinematic viscosity). Measurements, taken at 6 axial stations (Fig. 8), include total pressure (circular and flattened Pitot tubes and Kiel probes), static pressures (static pressure probes and wall pressure taps), mean-velocities and Reynolds-stresses (hot wires) and skin-friction (Preston tubes resting on the duct walls). These data [19] are available in digital form [24].

Because of the combined streamwise evolution of both cross-sectional form and area (Figs. 1, 8), the curvature of the duct's walls changes sign $x$-wise [54, Fig. 3, p. 241].

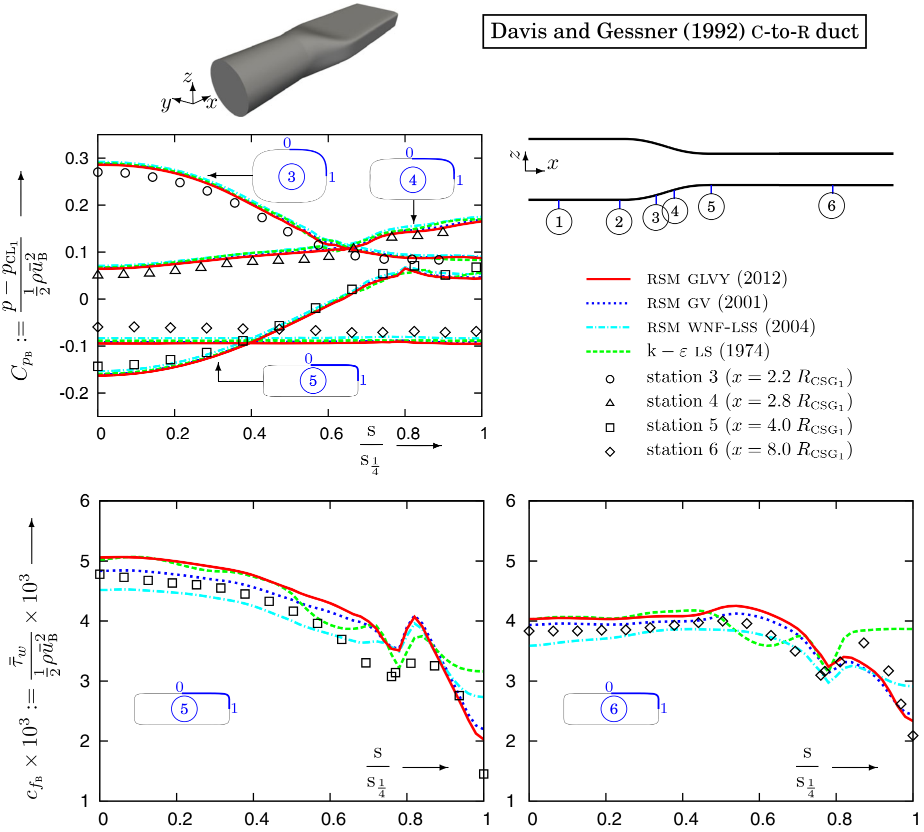

**Fig. 8** Comparison of measured [19] wall-pressure coefficient $C_{p_B}$ and skin-friction coefficient $c_{f_B}$, at 4 experimental measurement stations, with computations ($10 \times 10^6$ points grid discretizing the entire duct; Table 2) using (Section 2.1) the GV [35], the WNF–LSS [29] and the GLVY [28] RSMs, and the LS [51] linear k–ε model, for turbulent flow in a C-to-R transition duct ($Re_B = 390000$, $\bar{M}_{CL} \approxeq 0.09$; Table 3; s is the curvilinear coordinate of the duct contour in the $yz$-plane normalized by $\frac{1}{4}$ of the circumference $s_{\frac{1}{4}}$)

The upper and lower ($z$-wise) walls are concave from the inlet (station 2) to approximately midpoint (located between stations 3 and 4; Fig. 8) and then convex from approximately midpoint to exit (station 5; Fig. 8). The opposite applies to the sidewalls ($y$-wise) which are convex in the first part (from station 2 to approximately midpoint) then switching [54, Fig. 3, p. 241] to concave (from approximately midpoint to exit station 5). This streamwise evolution of the duct's geometry directly affects the mean pressure field, inducing strong pressure gradients, both streamwise (area change) and crossflow (wall curvature), generating intense ($\gtrapprox 10\ \%\ \bar{u}_B$; [19, Fig. 7, p. 371]) pressure-driven secondary flows [8, Prandtl's first kind] which rapidly form 2 contrarotating ($y$-wise symmetry) pairs of contrarotating ($z$-wise symmetry) vortices [19, Fig. 7, p. 371], one pair near the $z = 0$ midplane of each sidewall. Downstream of station 5 (exit of the transition section; Fig. 8) the vortex system persists, evolving streamwise, and is clearly visible at the last measurement station 6, 2 inlet diameters ($2D_{CSG_1}$) downstream of station 5 (Fig. 8).

The in-depth analysis of the experimental data by Davis [18] has largely contributed to our understanding of the dynamics of the mean-flow and associated Reynolds-stresses.

Careful computations of the Davis and Gessner [19] C-to-R transition duct, in quite satisfactory agreement with experimental measurements, have been reported by Sotiropoulos and Patel [73], using a 7-equation RSM, which is a variant of the Launder-Shima [52] RSM in 2 respects, (a) the use of the Hanjalić-Launder [46] closure for the triple velocity correlations in lieu of the Daly-Harlow [17] closure adopted for turbulent diffusion in the original model [52], and (b) the use of the modified coefficient-functions in the $\varepsilon$-equation introduced by Shima [68] to improve the prediction of skin-friction. Notice that the closure used for turbulent diffusion has a strong influence on the predicted secondary flows [77]. Sotiropoulos and Patel [75] have further exploited their computational results to analyse the streamwise ($x$-wise component of) mean-flow vorticity equation [75, (1), p. 504], and have shown that all of the vorticity-production mechanisms (vortex stretching and skewing, turbulence-induced production) are important in different regions of the flow.

The computations were run on a $10 \times 10^6$ grid (Table 2) discretizing the entire duct without symmetry conditions (Fig. 1). Based on the grid-convergence studies of Sotiropoulos and Patel [73], who used an $O(\Delta\ell^2)$ upwind numerical scheme for the incompressible RSM–RANS equations, this grid (Table 2) is sufficiently fine. As defined in the experimental study [18, 19], the origin of the coordinates system, $x = 0$, is located at mid-distance between station 1 and station 2, located at the beginning of the transition section ($x_1 = -R_{\text{CSG}_1}$, $x_2 = +R_{\text{CSG}_1}$; Fig. 8). The computational domain ($-D_{\text{CSG}_1} \leq x \leq 5D_{\text{CSG}_1}$) starts $\frac{3}{2}$ inlet-diameters ($\frac{3}{2}D_{\text{CSG}_1}$) upstream of the transition section inlet (station 2; Fig. 8) and extends 3 inlet-diameters ($3D_{\text{CSG}_1}$) downstream of the transition section exit (station 5; Fig. 8), to avoid interaction between the uniform outflow pressure boundary-condition and computed results at the last measurement station 6 located 2 inlet-diameters ($2D_{\text{CSG}_1}$) downstream of the transition section exit (Fig. 8). The grid is uniform in the streamwise ($x$) direction and consists of 2 blocks (Fig. 1; Table 2). The inner block (H$_\square$; Table 2) is an H-grid of $x$-wise varying square cross-section with uniform $yz$-spacing, introduced to avoid the axis-singularity of an axisymmetric-type grid. The outer block (O$_\square$; Table 2) is stretched geometrically near the wall with ratio $r_k$ (Table 2). For the investigated flow conditions, the first node at the walls is located at $\Delta n_w^+ \lessapprox \frac{2}{10}$ (Table 2), $n$ being the wall-normal direction.

At inflow (Table 3), measured [18, 19, 24] total conditions ($p_{t_{\text{CL}_\text{i}}} = 101325$ Pa, $T_{t_{\text{CL}_\text{i}}} = 298.3$ K), with a turbulent intensity $T_{u_{\text{CL}_\text{i}}} = 0.3\,\%$, were applied at the centerline. In the absence of experimental data, a turbulent lengthscale $\ell_{\text{T}_{\text{CL}_\text{i}}} = 50$ mm was assumed at the centerline, with reference to the duct radius ($R_{\text{CSG}_1} = 0.10215$ m) and the measured boundary-layer thickness $\delta_{995} = 30.85$ mm at station 1 (Fig. 8; Table 4). Detailed measurements of the boundary-layer profiles of mean-flow and Reynolds-stresses are available [18, 19, 24], and were interpolated onto the computational grid to define the inflow conditions. These data were extended to the wall, in the region where experimental data were not available, using semi-analytical profiles [30], and used to define, by assuming local equilibrium in the boundary-layer and matching to the prescribed centerline $\ell_{\text{T}_{\text{CL}_\text{i}}}$ [30], the $\varepsilon$ profiles. The outflow pressure was adjusted to obtain the correct $Re_\text{B} = 390000$ ($p_\text{o} = 100627$ Pa) corresponding to an inlet Mach number at centerline $M_{\text{CL}_\text{i}} \approxeq 0.0940$ (Table 3).

Computational results for the integral axisymmetric [25] boundary-layer thicknesses and associated shape-factors at the first measurement station 1 (Fig. 8), where the flow is still practically axisymmetric, are in good agreement (Table 4) with those determined from the experimental data [19, Table 1, p. 370]. Following Davis and Gessner [19] the approximate (linearized; $\delta \ll R_\text{CSG}$) definitions of the axisymmetric integral boundary-layer thicknesses [18, (3.5–3.7), p. 20], as expressed by Fujii and Okiishi [25], were applied.

Predicted wall-pressures are quite similar for all 4 turbulence models and are in quite satisfactory agreement with available measurements (Fig. 8). Skin-friction was measured by

**Table 4** Comparison of experimental inflow boundary-layer parameters, for the C-to-R transition duct [19, Table 1, p. 370] at station 1 located at $x = -R_{\mathrm{CSG}_1}$ (cross-sectional transition starts at $x = +R_{\mathrm{CSG}_1}$, one diameter downstream; Fig. 8) and for the S-duct [80, Table 2, p. 671] at station A located at $x = -R_{\mathrm{CSG}_\mathrm{A}}$ (centerline and cross-section evolution starts at $x = 0$, half a diameter downstream; Figs. 17 and 18), with computational results (grids Table 2) using the GLVY RSM [28], the GV RSM [35], the WNF–LSS RSM [29] and the LS k-$\varepsilon$ [51]

| Configuration | | Experiment | GLVY RSM | GV RSM | WNF–LSS RSM | LS k-$\varepsilon$ |
|---|---|---|---|---|---|---|
| C-to-R duct (station 1) | $\bar{u}_\mathrm{B}$ (m s$^{-1}$) | 29.95 | 30.20 | 30.25 | 30.41 | 30.51 |
| | $Re_\mathrm{B} \times 10^{-6}$ | 0.390 | 0.397 | 0.398 | 0.400 | 0.401 |
| | $\delta_{995}\ R_\mathrm{CSG}^{-1} \times 100$ | 28.55 | 30.03 | 30.05 | 29.95 | 28.98 |
| | $\delta_{1_{k_\mathrm{axi}}}\ R_\mathrm{CSG}^{-1} \times 100$ | 3.83 | 3.94 | 3.92 | 3.87 | 3.59 |
| | $\delta_{2_{k_\mathrm{axi}}}\ R_\mathrm{CSG}^{-1} \times 100$ | 2.81 | 2.93 | 2.92 | 2.90 | 2.69 |
| | $\delta_{3_{k_\mathrm{axi}}}\ R_\mathrm{CSG}^{-1} \times 100$ | 4.97 | 5.21 | 5.20 | 5.16 | 4.80 |
| | $H_{12_{k_\mathrm{axi}}}$ | 1.36 | 1.34 | 1.34 | 1.34 | 1.33 |
| | $H_{32_{k_\mathrm{axi}}}$ | 1.77 | 1.78 | 1.78 | 1.78 | 1.78 |
| S-duct (station A) | $\breve{M}_\mathrm{CL}$ | 0.6 | 0.59 | 0.60 | 0.60 | 0.62 |
| | $Re_\mathrm{CL} \times 10^{-6}$ | 2.6 | 2.58 | 2.59 | 2.62 | 2.67 |
| | $\delta_{95}\ R_\mathrm{CSG}^{-1} \times 100$ | 6.95 | 6.97 | 6.95 | 6.94 | 7.26 |
| | $\delta_{1_{k_\mathrm{axi}}}\ R_\mathrm{CSG}^{-1} \times 100$ | 1.46 | 1.11 | 1.10 | 1.11 | 1.13 |
| | $\delta_{2_{k_\mathrm{axi}}}\ R_\mathrm{CSG}^{-1} \times 100$ | 1.06 | 0.81 | 0.80 | 0.81 | 0.84 |
| | $\delta_{3_{k_\mathrm{axi}}}\ R_\mathrm{CSG}^{-1} \times 100$ | | 1.42 | 1.41 | 1.42 | 1.47 |
| | $H_{12_{k_\mathrm{axi}}}$ | 1.38 | 1.37 | 1.36 | 1.37 | 1.36 |
| | $H_{32_{k_\mathrm{axi}}}$ | | 1.75 | 1.76 | 1.76 | 1.76 |

$\bar{u}_\mathrm{B}$: bulk velocity; $R_\mathrm{CSG}$ ($D_\mathrm{CSG}$): casing radius (diameter); $Re_\mathrm{B} = \bar{u}_\mathrm{B} D_\mathrm{CSG} \nu^{-1}$: bulk Reynolds number ($\nu$ is the practically constant kinematic viscosity); $\delta_{995}$ ($\delta_{95}$): boundary-layer thickness measured from the wall to the location where the velocity is 99.5 % (95 %) of $\bar{u}_\mathrm{CL}$; $\delta_{1_{k_\mathrm{axi}}} = \int_0^\delta (1 - \bar{u}/\bar{u}_\mathrm{CL})\,(R/R_\mathrm{CSG}) d(R_\mathrm{CSG} - R)$: axisymmetric kinematic boundary-layer displacement-thickness; $\delta_{2_{k_\mathrm{axi}}} = \int_0^\delta (1 - \bar{u}/\bar{u}_\mathrm{CL})\,(\bar{u}/\bar{u}_\mathrm{CL})\,(R/R_\mathrm{CSG})\, d\,(R_\mathrm{CSG} - R)$ axisymmetric kinematic boundary-layer momentum-thickness; $\delta_{3_{k_\mathrm{axi}}} = \int_0^\delta \left(1 - \bar{u}^2/\bar{u}_\mathrm{CL}^2\right)(\bar{u}/\bar{u}_\mathrm{CL})\,(R/R_\mathrm{CSG})\, d\,(R_\mathrm{CSG} - R)$: axisymmetric kinematic boundary-layer energy-thickness; $H_{12_{k_\mathrm{axi}}} = \delta_{1_{k_\mathrm{axi}}}/\delta_{2_{k_{axi}}} \left(H_{32_{k_{axi}}} = \delta_{3_{k_\mathrm{axi}}}/\delta_{2_{k_\mathrm{axi}}}\right)$: axisymmetric kinematic boundary-layer shape-factors; $\breve{M}_\mathrm{CL} = \bar{u}_\mathrm{CL}/\breve{a}_\mathrm{CL}$: centerline Mach number ($\breve{a}_\mathrm{CL}$ is the centerline sound − speed); $R_{e_\mathrm{CL}} = \tilde{u}_\mathrm{CL} D_\mathrm{CSG} \nu_\mathrm{CL}^{-1}$: Reynolds number based on centerline flow quantities; axisymmetric integral boundary-layer thicknesses defined following Reichert [62, p. 67]

Preston tubes aligned with the $x$-wise direction and "*presumes that the 2-D form of the law-of-the-wall is valid and that streamwise pressure-gradients are small*" [18, p. 19]. Computed skin-friction was determined by the wall-normal gradient of streamwise velocity $\bar{u}$, at each measurement plane. At stations 5 (exit of the transition section) and 6 (2 inlet diameters further downstream), the GLVY and GV RSMs predict quite well the evolution of skin-friction along the peripheral wall-coordinate s (Fig. 8), yielding the correct s-gradient of $c_{f_\text{B}}$ everywhere. The small differences in absolute level at station 5 (Fig. 8), where the streamwise pressure-gradient is not negligible, are of the same order as the differences between measurements with Preston tubes of various diameters [19, Fig. 15, p. 374], and can also be attributed to the error introduced by the log-law assumption in the measurements [74]. On the other hand, the linear LS k–$\varepsilon$ model is unsatisfactory predicting a peculiar inverted s-curvature of $c_{f_\text{B}}$ around $\text{s} \approxeq 0.6\text{s}_{\frac{1}{4}}$ at both stations (Fig. 8) and a nearly constant level of $c_{f_\text{B}}$ on the sidewall ($0.9\text{s}_{\frac{1}{4}} \lessapprox s \lessapprox \text{s}_{\frac{1}{4}}$; Fig. 8). The negative s-gradient of $c_{f_\text{B}}$ on the sidewall ($\text{s} = \text{s}_{\frac{1}{4}}$ corresponds to the middle of the sidewall at $z = 0$; Fig. 8) is an important feature of the flow, as it is directly related [18, pp. 50–51] to the presence of the secondary flow streamwise vortices [19, Fig. 7, p. 371]. The overall prediction of $c_{f_\text{B}}$ by the WNF–LSS RSM is satisfactory, except for the too weak negative s-gradient of $c_{f_\text{B}}$ for $\text{s} \gtrapprox 0.9\text{s}_{\frac{1}{4}}$ (Fig. 8) which is indicative of an underestimation of the strength of the streamwise vortices.

All 4 turbulence models predict quite accurately the streamwise mean-flow velocity $\bar{u}$ along the $z$-traverse on the $y$-symmetry plane at all measurement stations (Fig. 9). Along the $y$-traverse on the $z$-symmetry plane (Fig. 9), differences between turbulence models start appearing at station 4, where the linear LS k–$\varepsilon$ model does not reproduce the experimentally observed inflection of the velocity profile at $y - y_w \approxeq 0.1 R_{\text{CSG}_1}$ (Fig. 9). Further downstream, at stations 5 and 6, the linear LS k–$\varepsilon$ model fails to predict the experimentally observed double inflection of the velocity profile along the $y$-traverse (Fig. 9), returning instead a more filled 2-D-boundary-layer-like profile. Davis [18, pp. 50–51] has identified this feature of the $\bar{u}$ velocity profile as the result of a "*transfer of low-momentum fluid from the boundary-layer toward the centerline creating a flat spot in the velocity field*", which "*is seen to be much larger at station 6 than at station 5*" (contour plots of $\bar{u}$; Fig. 9). This transfer, along the sidewall, is directly related to the presence of the secondary flow vortex-pair near the $z = 0$ symmetry plane [19, Fig. 7, p. 371]. The 3 RSMs successfully predict the double inflection of the $\bar{u}$ profile along the $y$-traverses at planes 5 and 6 (Fig. 9). The GLVY and GV RSMs agree quite well with measurements along the $y$-traverses at planes 5 and 6, indeed everywhere (Fig. 9). Although the WNF–LSS RSM predicts the double inflection shape of the $\bar{u}$ profile along the $y$-traverses at stations 5 and 6, it overpredicts $\bar{u}$, implying a slight underprediction of secondary flows.

Examination (Fig. 10) of the streamwise velocity profiles in wall-units ($\bar{u}^+ := u_\tau^{-1}\,\bar{u}$ *vs* $n^+ := u_\tau\, n\, \nu^{-1}$, where $n$ is the wall-normal distance and $u_\tau := \sqrt{\rho^{-1}\,\bar{\tau}_w}$ is the friction-velocity defined by the mean wall streamwise shear-stress $\bar{\tau}_w := \bar{\tau}_{xn}$) highlights the nonequilibrium conditions which prevail in the boundary-layers at the exit of the duct's transition section (station 5; Fig. 10) but also further downstream (station 6; Fig. 10). In addition to the outer flow data (Fig. 9) near-wall data were reported by Davis and Gessner [19, Fig. 16, p. 374] including both Pitot probe and hot wire measurements. These data, which are not available in digital or tabulated form, were digitized from [18, Fig. 5.47, p. 118]. This does introduce some uncertainty, especially in estimating the derivative $d_{n^+}\bar{u}^+$ which is required for the computation of the log-law diagnostic function $(n^+\, d_{n^+}\bar{u}^+)^{-1}$ [60]. Nonetheless, different sets of data (near-wall Pitot and hot wire, outer flow tabulated data, RSM computational results) yield similar conclusions (Fig. 10) concerning the validity of the log-law

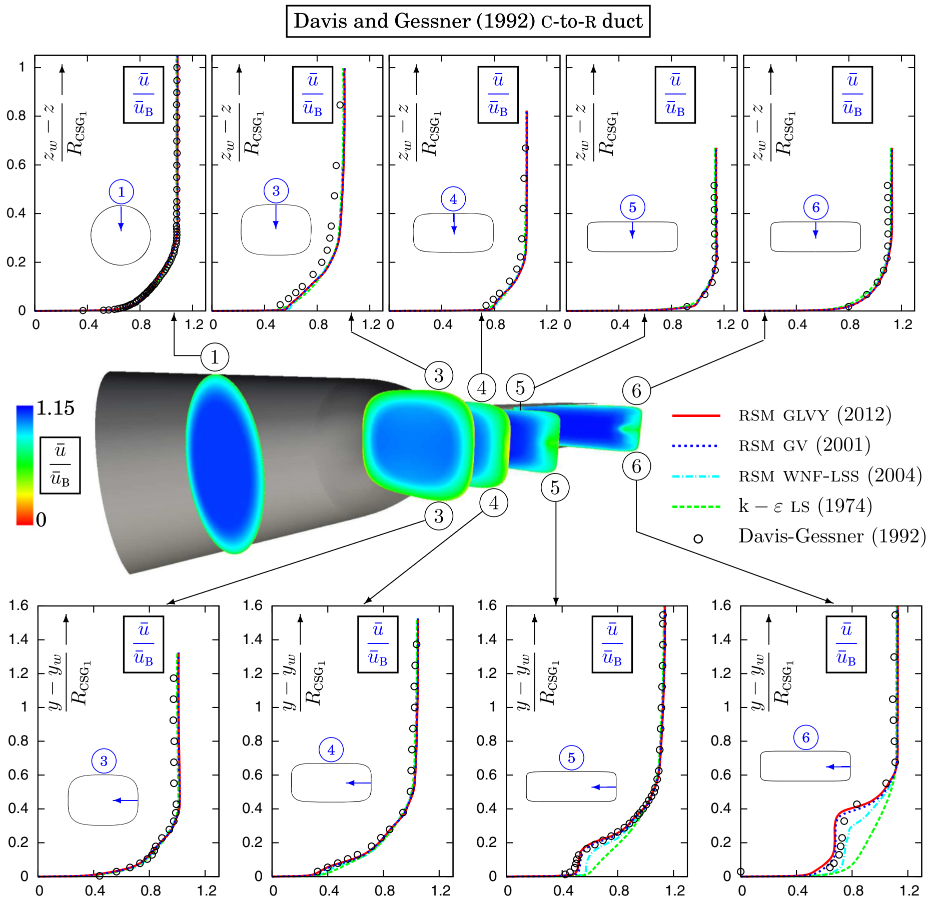

**Fig. 9** Comparison of measured [19] streamwise ($x$-wise) velocity $\bar{u}$, along the $y$-wise ($z = 0$ symmetry plane) and the $z$-wise ($y = 0$ symmetry plane) directions, at 5 experimental measurement stations, with computations ($10 \times 10^6$ points grid discretizing the entire duct; Table 2) using (Section 2.1) the GV [35], the WNF–LSS [29] and the GLVY [28] RSMs, and the LS [51] linear k–ε model, for turbulent flow in a C-to-R transition duct ($Re_{\mathrm{B}} = 390000$, $\bar{M}_{\mathrm{CL}} \approxeq 0.09$; Table 3; contour plots GLVY RSM)

in the overlap region [60]. Along the major axis ($y$-wise; $z = 0$ symmetry plane; Fig. 10), where the influence of the secondary-flow vortices [19, Fig. 7, p. 371] is strongest [18, pp. 50–51], differences in the level of $\bar{u}^+(y^+)$ are observed (Fig. 10) because of a $\sim$ 10 % difference between measured and predicted values of the skin-friction coefficient $c_{f_{\mathrm{B}}}$ at this location ($\mathrm{s} = \mathrm{s}_{\underline{1}}$; Fig. 8). This discrepancy in level does not affect the derivative $d_{y^+}\bar{u}^+$ and hence the log-law diagnostic function $(y^+ \, d_{y^+}\bar{u}^+)^{-1}$ which in presence of a log-law region should be approximately equal to the observed von Kàrmàn constant [60]. At the exit of the duct's transition section (station 5; Fig. 10) along the major axis ($y$-wise; $z = 0$ symmetry plane; Fig. 10), both measurements and computations clearly indicate that a log-law region is completely absent. Further downstream, (station 6 on the major axis; Fig. 10) both experimental data and RSM computations agree that there is no clearly defined log-law region where $(y^+ \, d_{y^+}\bar{u}^+)^{-1}$ is reasonably constant, implying that the flow has not yet recovered to equilibrium conditions at station 6, 2 inlet diameters ($2D_{\mathrm{CSG}_1}$) downstream of station 5

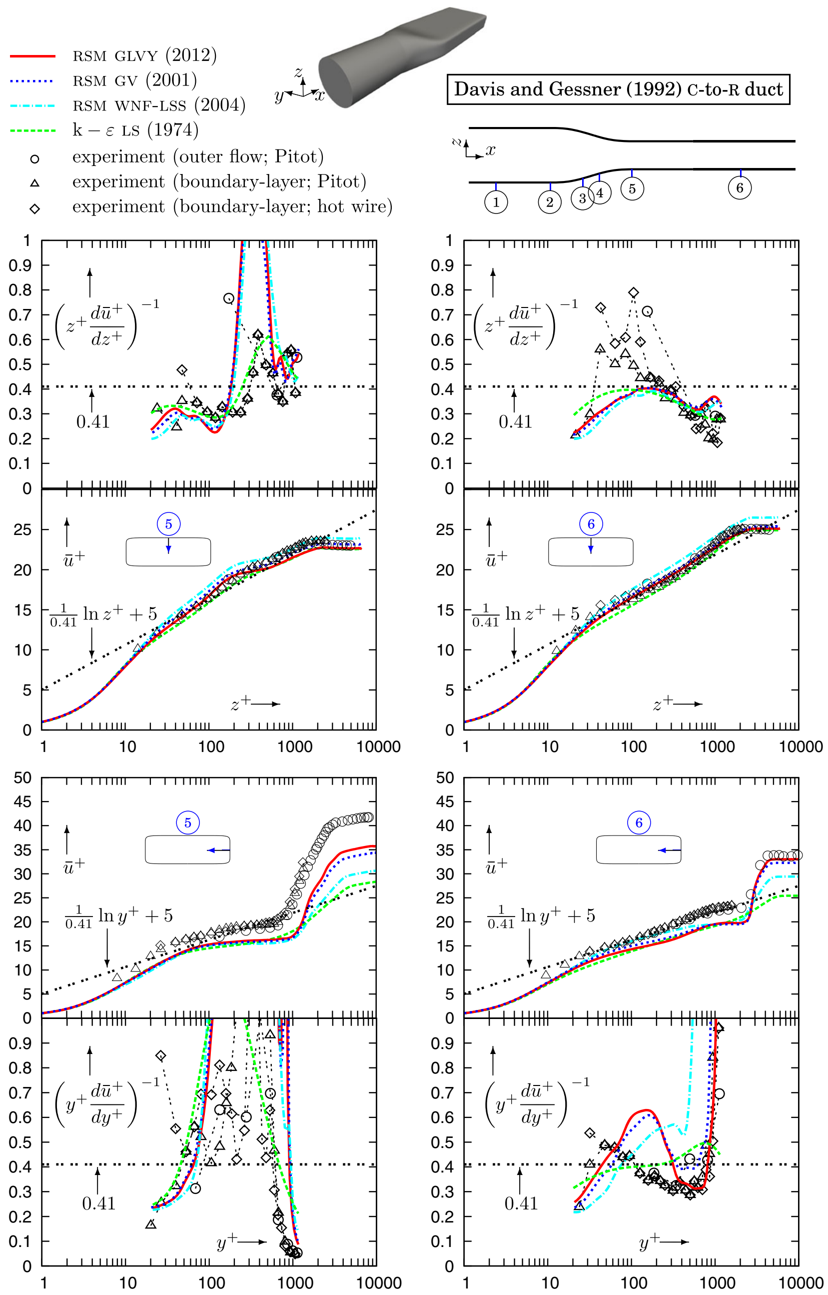

**Fig. 10** Comparison of measured [19] streamwise ($x$-wise) velocity-profiles in wall-units and log-law diagnostic functions [60], $\bar{u}^+(y^+)$ and $(y^+ d_{y^+}\bar{u}^+)^{-1}$ along the major axis ($z = 0$ symmetry plane), $\bar{u}^+(z^+)$ and $(z^+ d_{z^+}\bar{u}^+)^{-1}$ along the minor axis ($y = 0$ symmetry plane), at the last 2 experimental measurement stations, with computations ($10 \times 10^6$ points grid discretizing the entire duct; Table 2) using (Section 2.1) the GV [35], the WNF–LSS [29] and the GLVY [28] RSMs, and the LS [51] linear k–$\varepsilon$ model, for turbulent flow in a C-to-R transition duct ($Re_{\text{B}} = 390000$, $\bar{M}_{\text{CL}} \approxeq 0.09$; Table 3)

(exit of the transition section; Fig. 10). Notice also how much more severe (but also more precise) a test the log-law diagnostic function is, compared to the visual observation of the semi-logarithmic plots of $\bar{u}^+(y^+)$ (Fig. 10). Along the minor axis at the exit of the duct's transition section (station 5; $z$-wise; $y = 0$ symmetry plane; Fig. 10) again both experimental data and computations agree that there is no clearly defined log-law region, although departure from equilibrium is less pronounced than along the major axis (station 5; $y$-wise; $z = 0$ symmetry plane; Fig. 10). Even at the downstream station 6 along the minor axis (station 6; $z$-wise; $y = 0$ symmetry plane; Fig. 10) where the semi-logarithmic plot of $\bar{u}^+(z^+)$ seems to indicate the presence of a log-law region, the diagnostic function $(z^+ \, d_{z^+}\bar{u}^+)^{-1}$ reveals that this zone, if at all present, is still very limited. These observations (Fig. 10) imply that the flow remains at nonequilibrium conditions at station 6 ($2D_{\text{CSG}_1}$ downstream of the exit of the duct's transition section) where the observed secondary vortices [19, Fig. 7, p. 371] still influence the flow.

Differences between turbulence closures in predicting the wall-normal velocity $\bar{v}$ along the $y$-traverses at the $z = 0$ symmetry plane (where $\bar{w} = 0$ by symmetry) appear already at station 3 (Fig. 11). The GLVY and GV RSMs predict $\bar{v}$ quite accurately at stations 3 and 4, where the linear LS k–$\varepsilon$ model and to a lesser extent the WNF–LSS RSM, slightly overestimate it near the sidewall ($y - y_w \lessapprox 0.4R_{\text{CSG}_1}$; Fig. 11). At station 5, the 3 RSMs perform quite well in the outer part of the boundary-layer ($y - y_w \gtrapprox 0.2R_{\text{CSG}_1}$; Fig. 11) but underestimate the magnitude of $\bar{v}$ near the sidewall ($y - y_w \lessapprox 0.2R_{\text{CSG}_1}$; Fig. 11) by ~50 % at the peak. They are nonetheless in much better agreement with experimental data than the linear LS k–$\varepsilon$ model which predicts levels that are 5-fold lower ($y \lessapprox 0.4R_{\text{CSG}_1}$; station 5; Fig. 11). At station 6, 2 inlet diameters further downstream, the $\bar{v}$ velocity along the

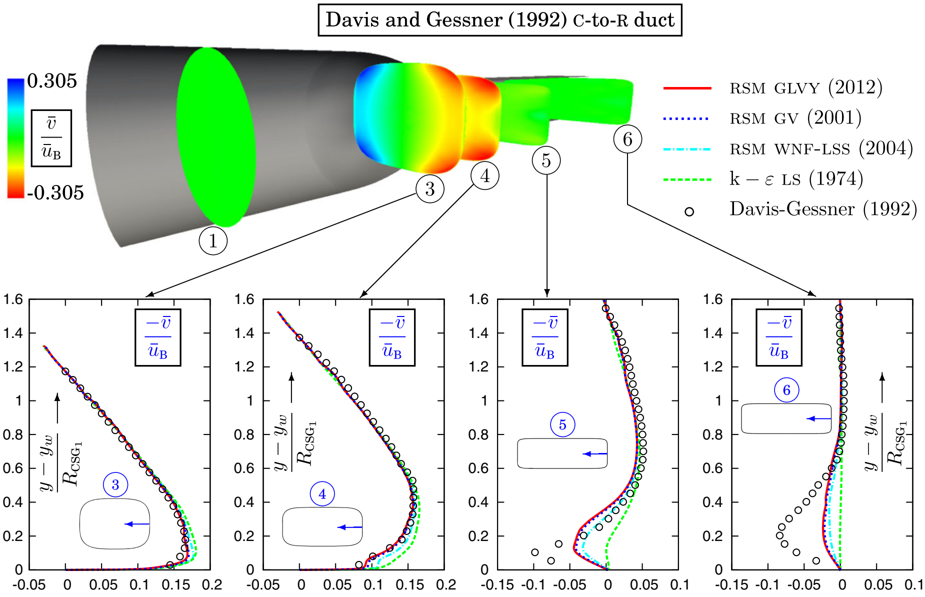

**Fig. 11** Comparison of measured [19] wall-normal velocity $\bar{v}$, along the $y$-wise ($z = 0$ symmetry plane) direction, at 4 experimental measurement stations, with computations ($10 \times 10^6$ points grid discretizing the entire duct; Table 2) using (Section 2.1) the GV [35], the WNF–LSS [29] and the GLVY [28] RSMs, and the LS [51] linear k–$\varepsilon$ model, for turbulent flow in a C-to-R transition duct ($Re_B = 390000$, $\bar{M}_{\text{CL}} \approxeq 0.09$; Table 3; contour plots GLVY RSM)

$y$-traverse is severely underestimated in magnitude by the 3 RSMs (Fig. 11) which underpredict the strength of the secondary flows at this station. Nonetheless, the 3 RSMs largely outperform the linear LS k–$\varepsilon$, which completely fails, returning negligibly small levels of $\bar{v}$ at station 6 (Fig. 11). The pair of contrarotating vortices observed at stations 5 and 6 near the intersection between the $z$-symmetry plane and the sidewall [19, Fig. 7, p. 371] induces velocities away from the sidewall ($\bar{v} < 0$ on the near-sidewall along the $y$-traverse; Fig. 11), whose measured peak value remains approximately constant ($\sim -0.1$) between stations 5 and 6 (Fig. 11). The failure of the RSM computations to correctly predict the relaxation of the flow in the straight constant cross-section duct between stations 5 and 6, possibly reveals an inadequacy of the models. Nonetheless, grid-resolution on the cross-section at these stations is rather poor (Fig. 1), containing only a few cells across the vortices [19, Fig. 7, p. 371]. For this reason, computations using locally finer meshes with an unstructured solver are required to determine computational grid-convergence of the flow in the contrarotating vortex pair region, and this will be the subject of future work. The wall-normal velocity $\bar{w}$ along the $z$-traverses at the $y = 0$ symmetry plane (where $\bar{v} = 0$ by symmetry) is very well predicted at all stations by all 4 turbulence closures (Fig. 12).

All 3 RSMs predict quite accurately the streamwise Reynolds-stress $\overline{u'u'}$ along the $z$-traverse on the $y = 0$ symmetry plane at station 5 (Fig. 13), and also, despite a slight underestimation, at station 6 (Fig. 13) further downstream. Along the $y$-traverse on the $z = 0$ symmetry plane, except for station 1 (Fig. 13) near the computational inflow where the measured Reynolds-stresses were interpolated onto the grid and applied as boundary conditions, the 3 RSMs predict correctly the profile shape but underestimate by $\sim$50 % the outer peak

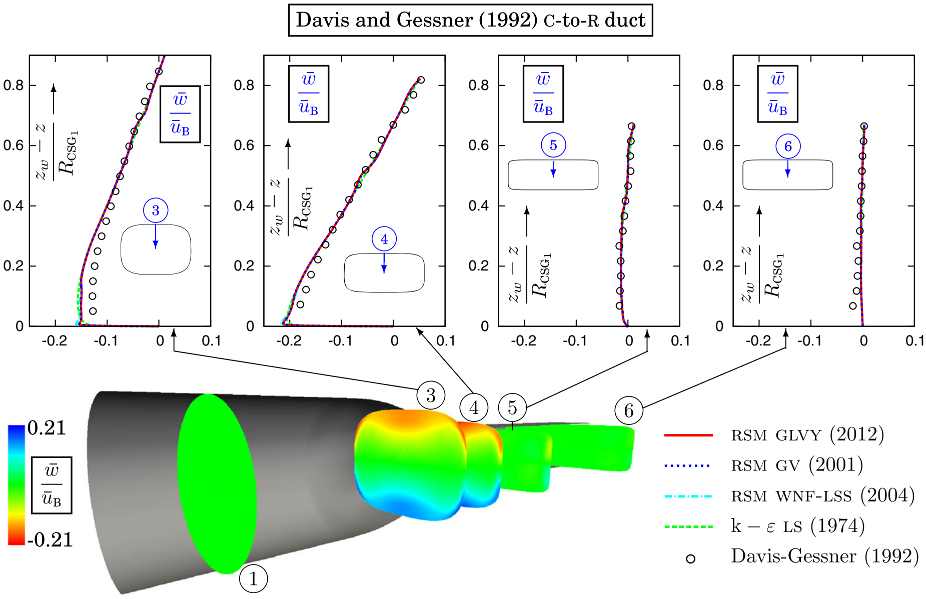

**Fig. 12** Comparison of measured [19] wall-normal velocity $\bar{w}$, along the $z$-wise ($y = 0$ symmetry plane) direction, at 4 experimental measurement stations, with computations ($10 \times 10^6$ points grid discretizing the entire duct; Table 2) using (Section 2.1) the GV [35], the WNF–LSS [29] and the GLVY [28] RSMs, and the LS [51] linear k–$\varepsilon$ model, for turbulent flow in a C-to-R transition duct ($Re_B = 390000$, $\bar{M}_{CL} \approxeq 0.09$; Table 3; contour plots GLVY RSM)

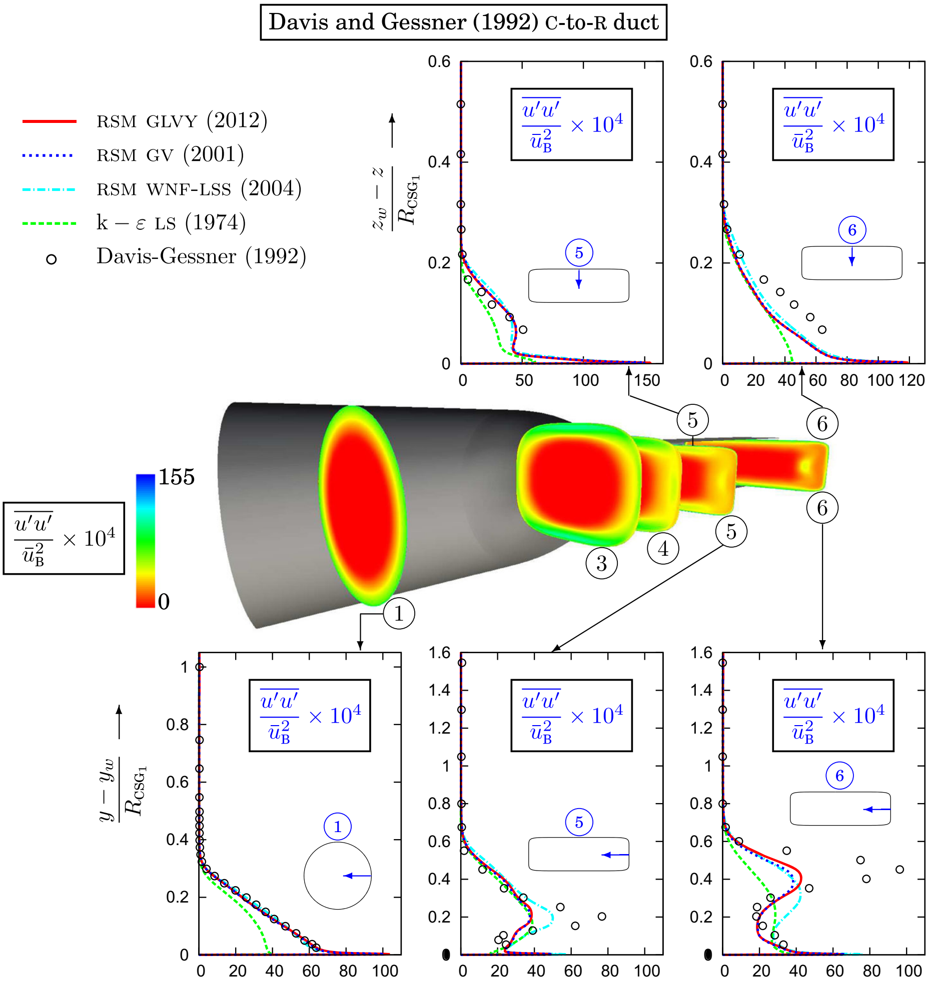

**Fig. 13** Comparison of measured [19] streamwise ($x$-wise) velocity-variance $\overline{u'u'}$, along the $y$-wise ($z = 0$ symmetry plane) and the $z$-wise ($y = 0$ symmetry plane) directions, at 3 experimental measurement stations, with computations ($10 \times 10^6$ points grid discretizing the entire duct; Table 2) using (Section 2.1) the GV [35], the WNF–LSS [29] and the GLVY [28] RSMs, and the LS [51] linear k–$\varepsilon$ model, for turbulent flow in a C-to-R transition duct ($Re_B = 390000$, $\bar{M}_{CL} \approxeq 0.09$; Table 3; contour plots GLVY RSM)

value at stations 5 and 6 (Fig. 13). All 3 RSMs predict quite accurately the in-plane diagonal Reynolds-stresses $\overline{v'v'}$ (Fig. 14) and $\overline{w'w'}$ (Fig. 15), with the exception of $\overline{v'v'}$ at station 6 along the $y$-traverse on the $z$-symmetry plane (Fig. 15) where the outer peak value is underestimated by ∼50 %. The predictions of the diagonal Reynolds-stresses ($\overline{u'u'}$, $\overline{v'v'}$, $\overline{w'w'}$) by the GLVY and GV RSMs are in very close agreement (Figs. 13–15), and also with those predicted by WNF–LSS RSM (Figs. 13–15) except at station 6 along the $y$-traverse on the $z$-symmetry plane where the GLVY and GV RSMs are in closer agreement with measurements. Expectedly, the linear k–$\varepsilon$ model completely fails in predicting the Reynolds-stress tensor anisotropy, yielding unsatisfactory results for the diagonal Reynolds-stresses (Figs. 13–15), because of the pathological shortcomings of the Boussinesq hypothesis [82, pp. 273–278].

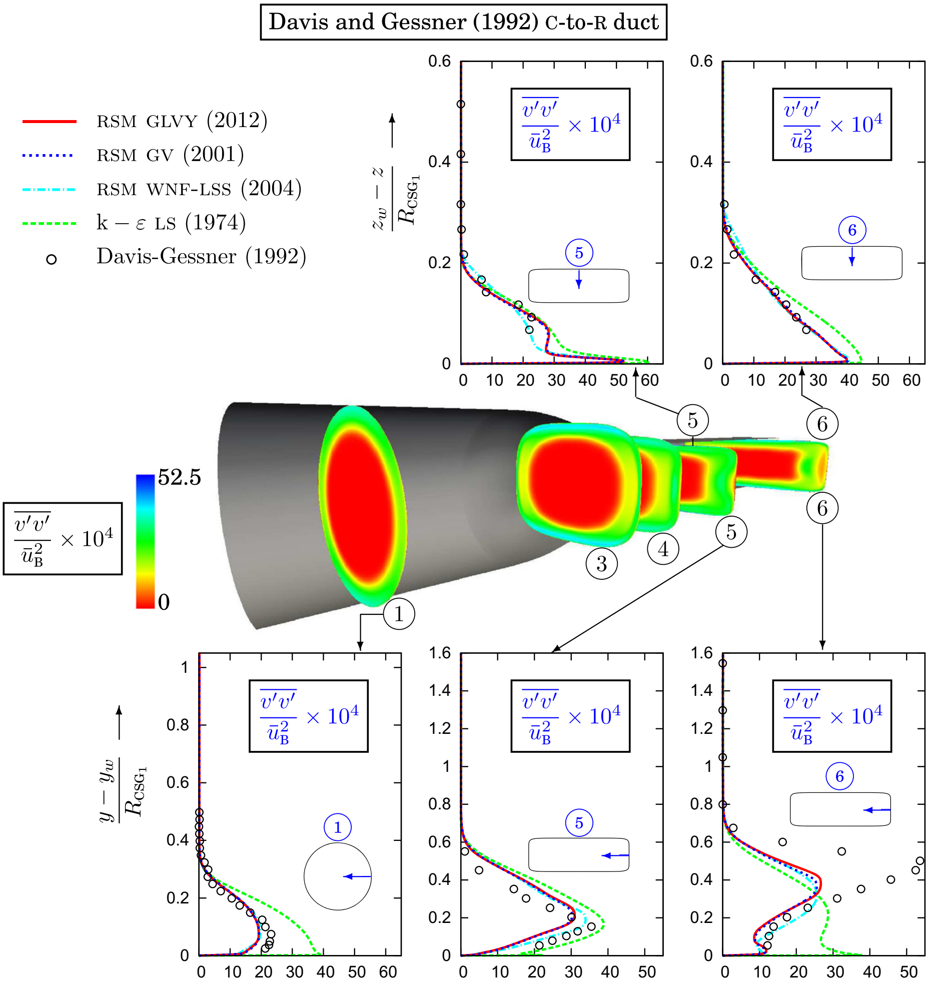

**Fig. 14** Comparison of measured [19] $y$-wise velocity-variance $\overline{v'v'}$, wall-normal along the $y$-wise ($z = 0$ symmetry plane) direction and transverse along the $z$-wise ($y = 0$ symmetry plane) direction, at 3 experimental measurement stations, with computations ($10 \times 10^6$ points grid discretizing the entire duct; Table 2) using (Section 2.1) the GV [35], the WNF–LSS [29] and the GLVY [28] RSMs, and the LS [51] linear k–$\varepsilon$ model, for turbulent flow in a C-to-R transition duct ($Re_B = 390000$, $\bar{M}_{CL} \approxeq 0.09$; Table 3; contour plots GLVY RSM)

The prediction of the shear Reynolds-stress $\overline{w'u'}$ along the $z$-traverse on the $y$-symmetry plane (where $\overline{u'v'} = 0$ by symmetry) at stations 5 and 6 by the 3 RSMs is quite satisfactory (Fig. 16). On the contrary, the LS [51] linear k–$\varepsilon$ model does not reproduce as well the shape of the $\overline{w'u'}$ profile at station 5 (Fig. 16), a deficiency which does not appear to have a substantial influence on the prediction of the streamwise mean-velocity profile $\bar{u}$ ($z$-traverse, station 5, Fig. 9). The prediction of the shear Reynolds-stress $\overline{u'v'}$ (Fig. 16) along the $y$-traverse on the $z$-symmetry plane (where $\overline{u'w'} = 0$ by symmetry) should be analyzed in relation to the prediction of the streamwise mean-velocity $\bar{u}$ (Fig. 9). At station 6, along the $y$-traverse on the $z$-symmetry plane, all turbulence models underestimate by ~50 % the outer peak of $\overline{u'v'}$ at $y - y_w \approxeq 0.45 R_{CSG_1}$ (Fig. 16). The grid-resolution issues mentioned

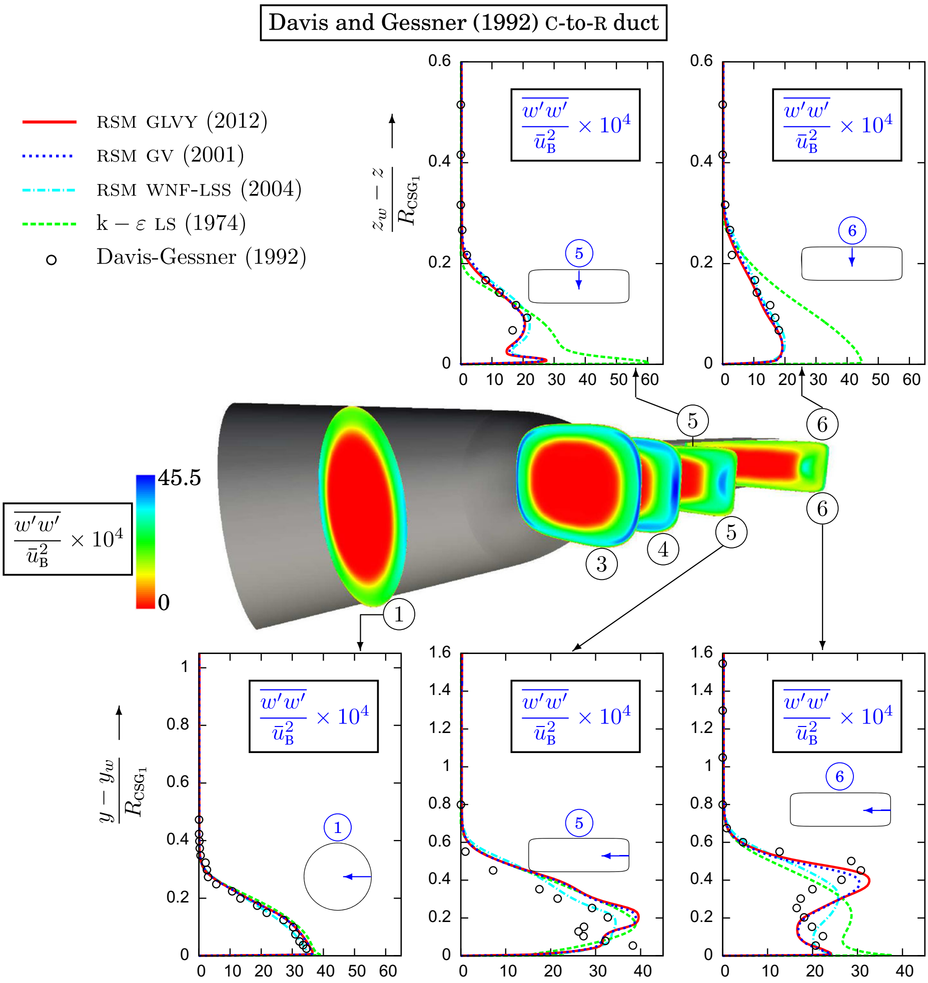

**Fig. 15** Comparison of measured [19] $z$-wise velocity-variance $\overline{w'w'}$, transverse along the $y$-wise ($z = 0$ symmetry plane) direction and wall-normal along the $z$-wise ($y = 0$ symmetry plane) direction, at 3 experimental measurement stations, with computations ($10 \times 10^6$ points grid discretizing the entire duct; Table 2) using (Section 2.1) the GV [35], the WNF–LSS [29] and the GLVY [28] RSMs, and the LS [51] linear k–$\varepsilon$ model, for turbulent flow in a C-to-R transition duct ($Re_B = 390000$, $\bar{M}_{CL} \approxeq 0.09$; Table 3; contour plots GLVY RSM)

above not withstanding, notice that the GLVY and GV RSMs predict reasonably well $\overline{u'v'}$ at station 6 for $0 \lessapprox y - y_w \lessapprox 0.3R_{\text{CSG}_1}$ (Fig. 16), and this is obviously related to the satisfactory prediction of $\bar{u}$ by these models ($y$-traverse, station 6; Fig. 9). On the contrary, the linear LS k–$\varepsilon$ model which strongly overpredicts $\overline{u'v'}$ in this range ($y$-traverse, $0 \lessapprox y - y_w \lessapprox 0.3R_{\text{CSG}_1}$, station 5; Fig. 16) fails to correctly predict the streamwise mean-velocity $\bar{u}$ at this location (Fig. 9). Notice that the WNF–LSS RSM which performs much better than the LS k–$\varepsilon$ model in predicting the shear Reynolds-stress $\overline{u'v'}$ ($y$-traverse, $0 \lessapprox y - y_w \lessapprox 0.3R_{\text{CSG}_1}$, station 6; Fig. 16) also predicts the correct double inflection shape of the $\bar{u}$-profile ($y$-traverse, station 6; Fig. 9), albeit less accurately than the GLVY and GV RSMs.

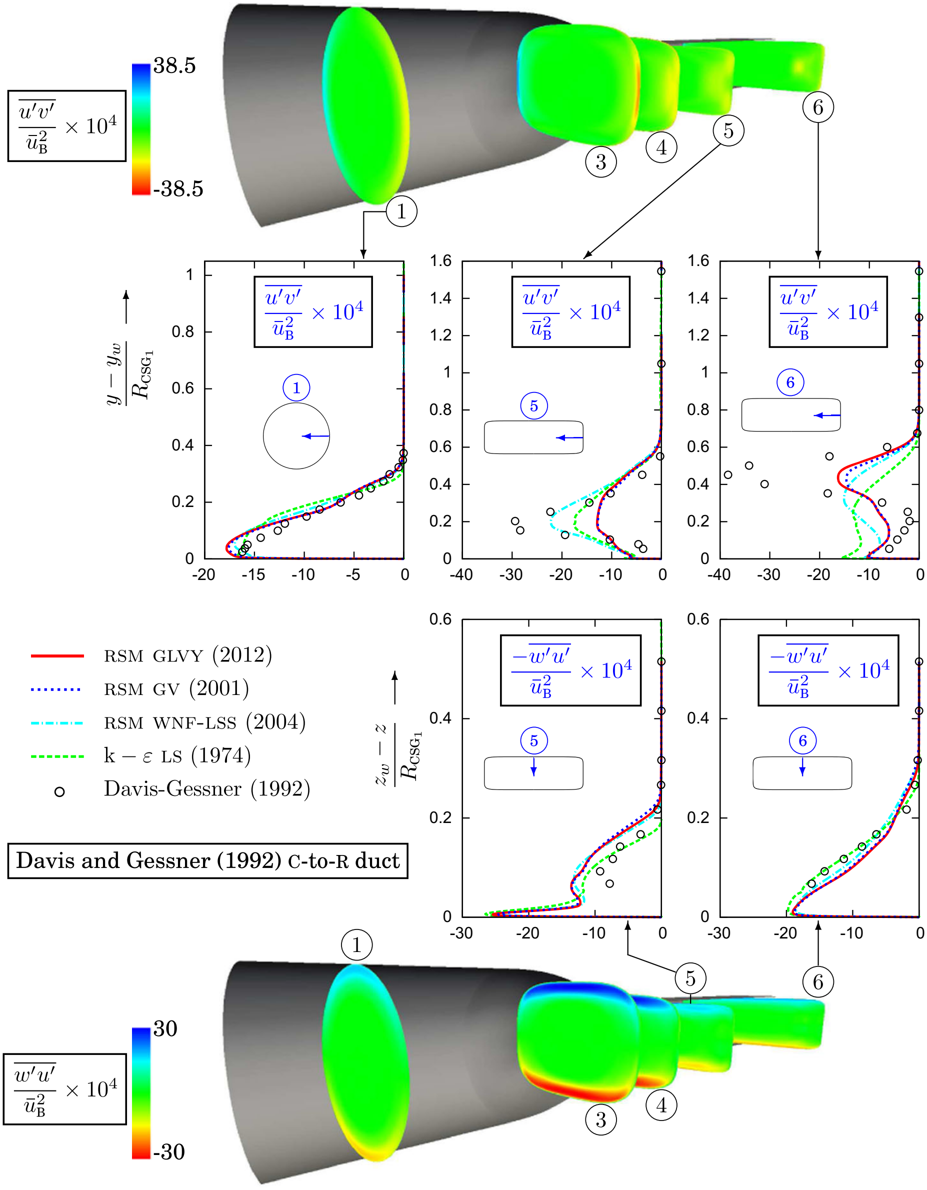

**Fig. 16** Comparison of measured [19] shear Reynolds-stress, $\overline{u'v'}$ along the $y$-wise ($z = 0$ symmetry plane) and $\overline{u'w'}$ the $z$-wise ($y = 0$ symmetry plane) directions, at 3 experimental measurement stations, with computations ($10 \times 10^6$ points grid discretizing the entire duct; Table 2) using (Section 2.1) the GV [35], the WNF–LSS [29] and the GLVY [28] RSMs, and the LS [51] linear k–ε model, for turbulent flow in a C-to-R transition duct ($Re_B = 390000$, $\bar{M}_{CL} \approxeq 0.09$; Table 3; contour plots GLVY RSM)

Despite the grid-convergence issues raised above (which can only be resolved by additional calculations on much finer grids), the systematic comparison of the computations of the Davis and Gessner [19] C-to-R duct configuration with the experimental data

(Figs. 8–16) yields useful conclusions. The linear LS k–$\varepsilon$ model, handicapped by Boussinesq's hypothesis [82, pp. 273–279] fails to predict with sufficient accuracy the regions of the flowfield that are dominated by secondary flows (Figs. 8–16). The 3 RSMs perform much better, capturing several complex features of the flow (Figs. 8–16), although they are not sufficiently accurate on the $10 \times 10^6$ points grid used (Table 2) in predicting all the details of the flow near the intersection of the sidewall with the $z = 0$ symmetry plane (Figs. 8–16). As for the Gessner and Emery [39] square duct case (Section 3.1), the GLVY and GV RSMs (which yield very similar results) perform sometimes better than the WNF–LSS RSM, especially near the sidewall in the region of strong secondary flows.

### 3.3 Diffusing 3-D S-Duct [80]

The previously studied square duct (Section 3.1) and C-to-R transition duct (Section 3.2) test-cases have a straight centerline ($x$-axis of the coordinates system). Furthermore, the diverging part of the C-to-R transition duct (from station 2 to midpoint of the transition section; Fig. 8) was sufficiently long to avoid separation. The S-duct test-case [79, 80] includes these 2 features, *viz* it has a serpentine centerline (S-duct) combined with substantial (52 %) area increase, from inflow to outflow [80], inducing a large region of separated flow near the duct floor, immediately after the beginning of the S-bend (Fig. 17). The serpentine centerline of the S-duct lies on the $xz$-plane (no off-plane skewing; Fig. 18) and consists of 2 circular arcs of opposite curvature smoothly joined at a common tangency point [80, Fig. 2, p. 670]. Planes ⊥ to the centerline define stations of circular cross-section,

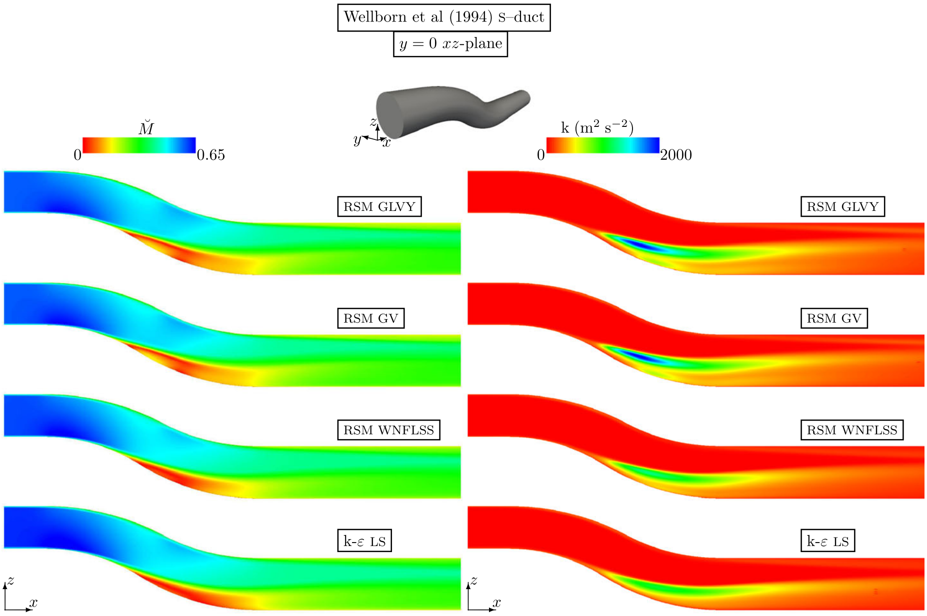

**Fig. 17** Level plots of Mach number $\breve{M}$ and of turbulent kinetic energy k on the $y = 0$ symmetry plane of the Wellborn et al. [80] diffusing S-duct ($Re_{\text{CL}_\text{A}} = 2.6 \times 10^6$, $\bar{M}_{\text{CL}_\text{A}} \approxeq 0.6$; Table 3) obtained from computations ($2 \times 10^6$ points grid discretizing the entire duct; Table 2) using (Section 2.1) the GV [35], the WNF–LSS [29] and the GLVY [28] RSMs, and the LS [51] linear k–$\varepsilon$ model

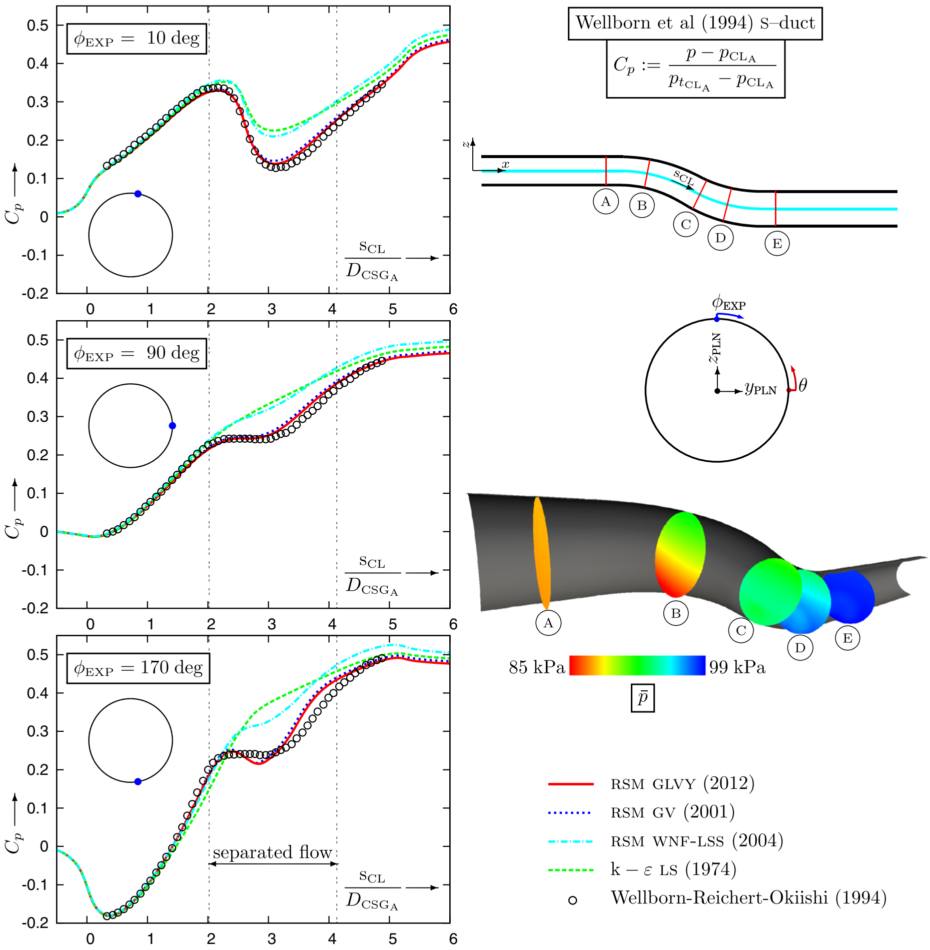

**Fig. 18** Comparison of measured [80] wall-pressure coefficient $C_p$ (based on centerline quantities at plane A), plotted against the curvilinear coordinate $s_{\text{CL}}$ along the duct centerline (planes $\perp$ to the centerline define stations of circular cross-section), at 3 azimuthal locations, with computations ($2 \times 10^6$ points grid discretizing the entire duct; Table 2) using (Section 2.1) the GV [35], the WNF–LSS [29] and the GLVY [28] RSMs, and the LS [51] linear k–ε model, for turbulent flow in a diffusing S-duct ($Re_{\text{CL}_\text{A}} = 2.6 \times 10^6$, $\bar{M}_{\text{CL}_\text{A}} \approxeq 0.6$; Table 3; contour plots GLVY RSM)

with varying radius, whose dependence on the angular coordinate (equivalently the curvilinear length) along the centerline [80, (2), p. 670] defines the geometry of the duct. The origin of the curvilinear coordinates along the centerline $s_{\text{CL}}$ is at the beginning of the S-bend, which also corresponds to $x = 0$. The inlet-diameter is $D_{\text{CSG}_\text{A}} = 2R_{\text{CSG}_\text{A}} = 0.2042$ m (this is also the diameter at the first measurement plane A, located at $x = -\frac{1}{2}D_{\text{CSG}_\text{A}}$, 1 inlet-radius upstream of the beginning of the S-bend; Fig. 18) while the exit diameter is $D_{\text{CSG}_\text{E}} = 0.2514$ m (this is also the diameter at the last measurement plane E, located at $x \approxeq 5.61D_{\text{CSG}_\text{A}}$, 0.61 inlet-diameters downstream of the exit of the S-bend located at $x = 5D_{\text{CSG}_\text{A}}$; Fig. 18).

The flow [80] is subsonic (centerline Mach number at measurement plane A $\bar{M}_{\mathrm{CL_A}} \approxeq 0.60$) and the centerline Reynolds number is $Re_{\mathrm{CL_A}} \approxeq 2.6\times 10^6$ ($Re_{\mathrm{CL_A}} = \bar{u}_{\mathrm{CL_A}} D_{\mathrm{CSG_A}} \bar{\nu}_{\mathrm{CL_A}}^{-1}$, where $\bar{u}_{\mathrm{CL_A}}$ is the centerline velocity and $\bar{\nu}_{\mathrm{CL_A}}$ is the kinematic viscosity at centerline). Available field measurements, taken at 5 axial planes ⊥ to the centerline (circular cross-section; Fig. 18), using calibrated 3-hole and 5-hole pneumatic probes [79, 80], provide pressures (total and static) and the mean-flow velocity vectors. Wall-pressure measurements are also available [79, 80], both around the circumference of 4 of the measurement planes (Fig. 19), and streamwise, at 3 angular locations (Fig. 18).

The computations were run on a $2\times 10^6$ grid (Table 2) discretizing the entire duct without symmetry conditions (Fig. 1). Based on previous grid-convergence studies [26], on a similar 2S-duct configuration (for the twice longer 2S-duct [26] computations with the GV RSM on meshes of $2.3 \times 10^6$ and $6.2 \times 10^6$ yielded quite similar results), this grid (Table 2) is sufficient to obtain accurate results for comparison between the different models (Section 2.1). The computational domain ($-0.98 D_{\mathrm{CSG_A}} \lessapprox x \lessapprox 9.8 D_{\mathrm{CSG_A}}$) starts approximately 1 inlet-diameter ($D_{\mathrm{CSG_A}}$) upstream of the start of the S-bend and extends approximately

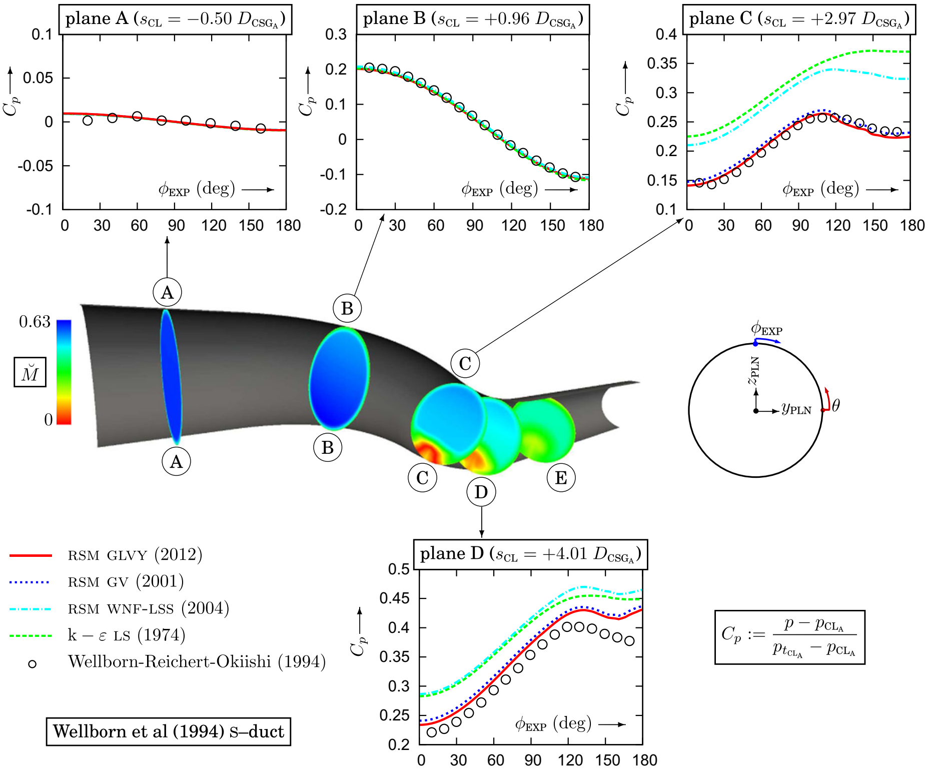

**Fig. 19** Comparison of measured [80] wall-pressure coefficient $C_p$ (based on centerline quantities at plane A), at 4 experimental measurement stations (planes ⊥ to the centerline whose intersection with the duct defines circular cross-sections), plotted against the azimuthal location along the circumference, with computations ($2 \times 10^6$ points grid discretizing the entire duct; Table 2) using (Section 2.1) the GV [35], the WNF–LSS [29] and the GLVY [28] RSMs, and the LS [51] linear k–ε model, for turbulent flow in a diffusing S-duct ($Re_{\mathrm{CL_A}} = 2.6 \times 10^6$, $\bar{M}_{\mathrm{CL_A}} \approxeq 0.6$; Table 3; $s_{\mathrm{CL}}$ is the curvilinear coordinate along the duct centerline; contour plots GLVY RSM)

5 inlet-diameters ($5D_{\mathrm{CSG_A}}$) downstream of the S-bend exit, thus avoiding any interaction between the uniform outflow pressure boundary-condition and computed results at the last measurement station E (Fig. 8). The grid is uniform in the streamwise ($x$) direction (the $i = \text{const}$ grid-surfaces are $\perp x$ planes) and consists of 2 blocks (Fig. 1; Table 2). The inner block (H$\square$; Table 2) is an H-grid of $x$-wise varying square cross-section with uniform $yz$-spacing, introduced to avoid the axis-singularity of an axisymmetric-type grid. The outer block (O$\square$; Table 2) is stretched geometrically near the wall with ratio $r_k$ (Table 2). For the investigated flow conditions, the first node at the walls is located at $\Delta n_w^+ \lessapprox \frac{4}{10}$ (Table 2), $n$ being the wall-normal direction.

At inflow (Table 3) total conditions ($p_{t_{\mathrm{CL_i}}} = 111330$ Pa, $T_{t_{\mathrm{CL_i}}} = 296.4$ K) were assumed at the centerline, corresponding to the Mach ($M_{\mathrm{CL_i}} = 0.60$) and Reynolds ($Re_{\mathrm{CL_i}} = 2.6 \times 10^6$) number values reported in the measurements [79, 80]. A turbulent intensity $T_{u_{\mathrm{CL_i}}} = 0.63\,\%$ was applied at the centerline; Wellborn et al. [79, p. 29] report this value from measurements of Reichert [62] on the same facility. In the absence of experimental data, a turbulent lengthscale $\ell_{\mathrm{T_{CL_i}}} = 50$ mm was assumed at the centerline, with reference to the duct radius ($R_{\mathrm{CSG_A}} = 0.1021$ m). The initial inflow boundary-layer thickness and Coles-parameter [30] were adjusted, independently for each model (Table 3), to match the experimental boundary-layer data at the first measurement plane A. Finally the outflow pressure was also adjusted, independently for each model (Table 3), to obtain the correct $\check{M}_{\mathrm{CL_A}} \approxeq 0.60$ (Table 4).

Computational results for the integral axisymmetric [25] boundary-layer thicknesses and associated shape-factors at the first measurement plane A (Fig. 8), where the flow is still practically axisymmetric, are in good agreement (Table 4) with those determined from the experimental data [80, Table 2, p. 671]. Following Wellborn et al. [79] the approximate (linearized; $\delta \ll R_{\mathrm{CSG}}$) definitions of the axisymmetric integral boundary-layer thicknesses [79, (V.1–V.2), p.29], as expressed by Fujii and Okiishi [25], were applied. The definitions given by Wellborn et al. [79, (V.1–V.2), p.29] concern compressible integral thicknesses, but the actual shape-factor values ($\sim$1.38) imply that the thicknesses provided in the experimental database [79, 80] are kinematic (the corresponding compressible value would be $\sim$1.65), as defined in the associated study (from which the inlet turbulent intensity was determined), on the same experimental facility, by Reichert [62, (V.7–V.8), p. 67]. This is implied by the statement that "*comparisons indicate little deviation from a conventional turbulent boundary-layer*" [79, p. 29].

All 4 turbulence closures predict separation near the duct floor (Fig. 17) in agreement with experiment [80], but differ in the location of separation and reattachment, in the extent ($x$-wise) and thickness ($z$-wise) of the separated flow region, and in the predicted structure of the recirculating flow (Fig. 17). The GLVY and GV RSMs yield very similar results (Fig. 17), and are in quite satisfactory agreement with available measurements (Figs. 18–24). The WNF–LSS RSM predicts separation further downstream (with respect to the GLVY and GV RSMs; Fig. 17) and the linear LS k–$\varepsilon$ model, which is known to underestimate flow detachment [35], separates a little further downstream still. Even more important, there are noticeable differences in the separated flow structure (Fig. 17) between the GLVY and GV RSMs on the one hand, and the WNF–LSS RSM and the linear LS k–$\varepsilon$ model on the other. The GLVY and GV RSMs predict a much thicker ($z$-wise) low-speed region with a stronger recirculation zone near the wall just downstream of separation (Fig. 17). This flow structure contains strong mean-velocity gradients producing high levels of turbulent kinetic energy k, which presents 2 local maxima, one in the post-separation wake-region (dark blue levels, GLVY and GV RSMs; Fig. 17) and another near the wall in the pre-reattachment region (light green levels of k, GLVY and GV RSMs; Fig. 17). On the other hand, the WNF–LSS RSM and

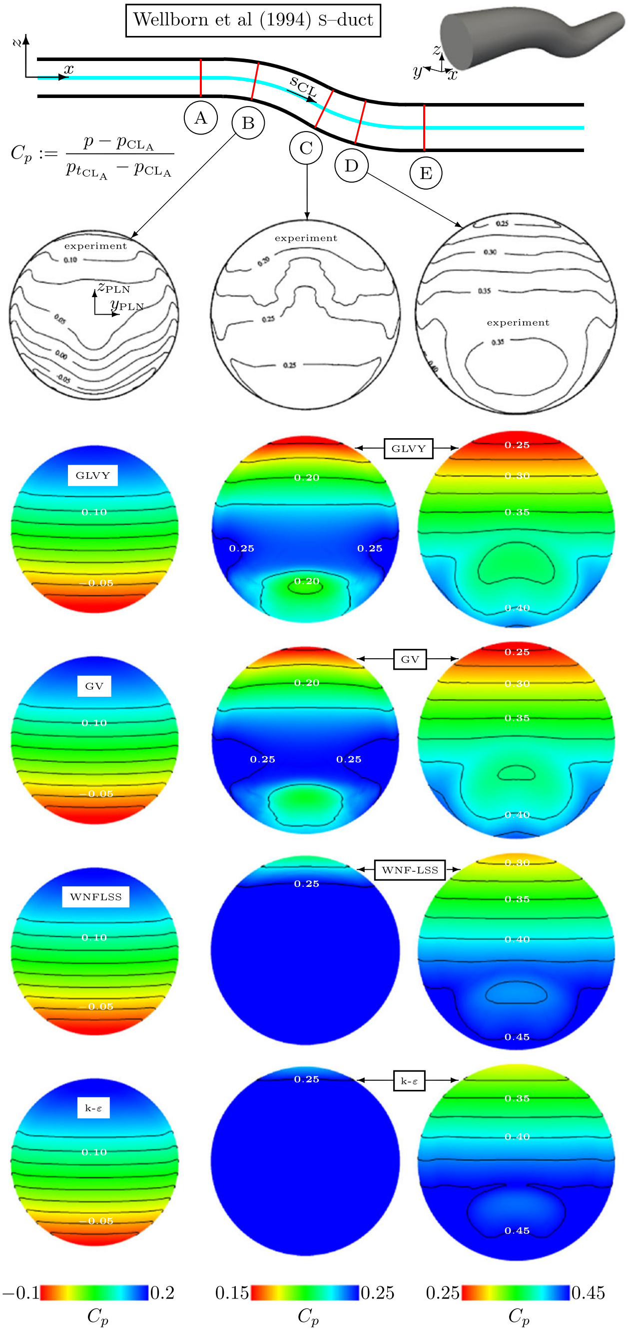

**Fig. 20** Comparison, at 3 measurement planes (planes ⊥ to the centerline define stations of circular cross-section), of experimental [80] contours of pressure coefficient $C_p$ (based on centerline quantities at plane A; contour step 0.025), with computations ($2 \times 10^6$ points grid discretizing the entire duct; Table 2) using (Section 2.1) the GV [35], the WNF–LSS [29] and the GLVY [28] RSMs, and the LS [51] linear k–$\varepsilon$ model ($Re_{\mathrm{CL_A}} = 2.6 \times 10^6$, $\bar{M}_{\mathrm{CL_A}} \approxeq 0.6$; Table 3)

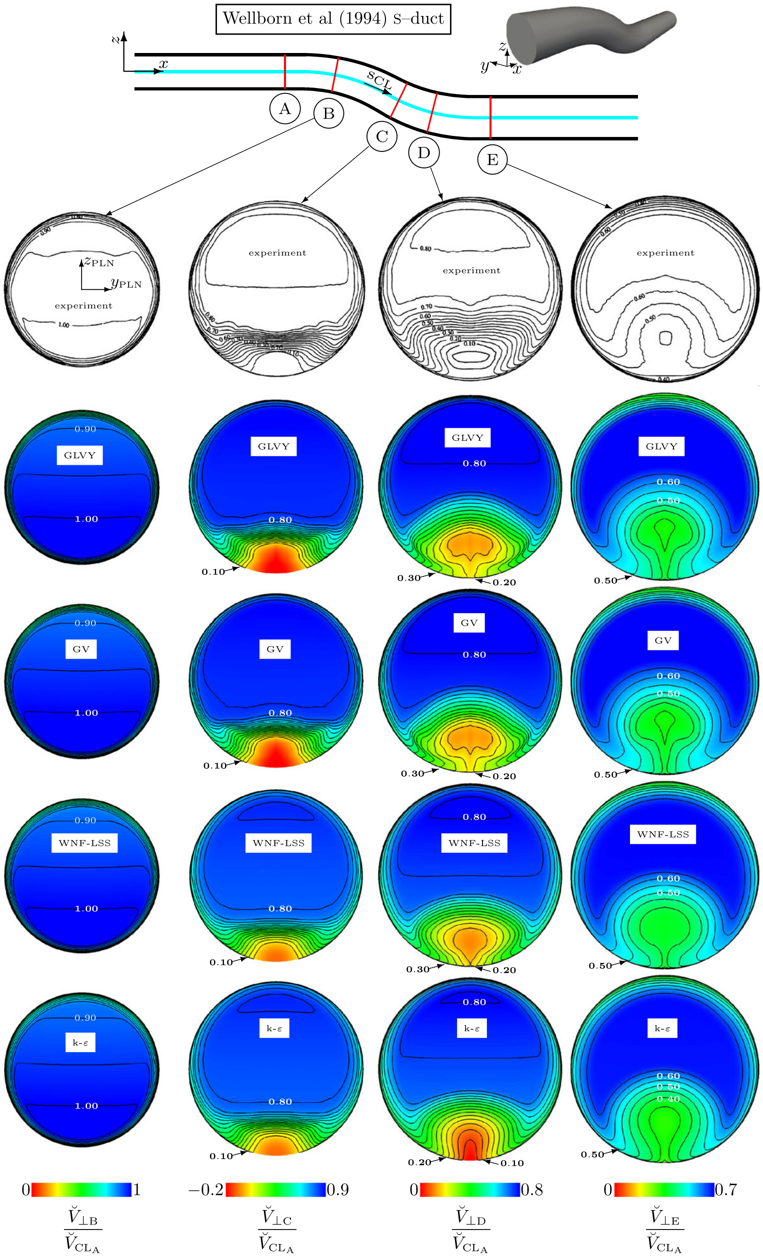

**Fig. 21** Comparison, at 4 measurement planes (planes ⊥ to the centerline define stations of circular cross-section), of experimental [80] contours of normal-to-the-plane (streamwise) velocity $\breve{V}_{\perp}$ (made nondimensional by the centerline velocity at plane A, $\breve{V}_{\text{CL}_\text{A}}$; contour step 0.05), with computations ($2 \times 10^6$ points grid discretizing the entire duct; Table 2) using (Section 2.1) the GV [35], the WNF–LSS [29] and the GLVY [28] RSMs, and the LS [51] linear k–$\varepsilon$ model ($Re_{\text{CL}_\text{A}} = 2.6 \times 10^6$, $\bar{M}_{\text{CL}_\text{A}} \approxeq 0.6$; Table 3)

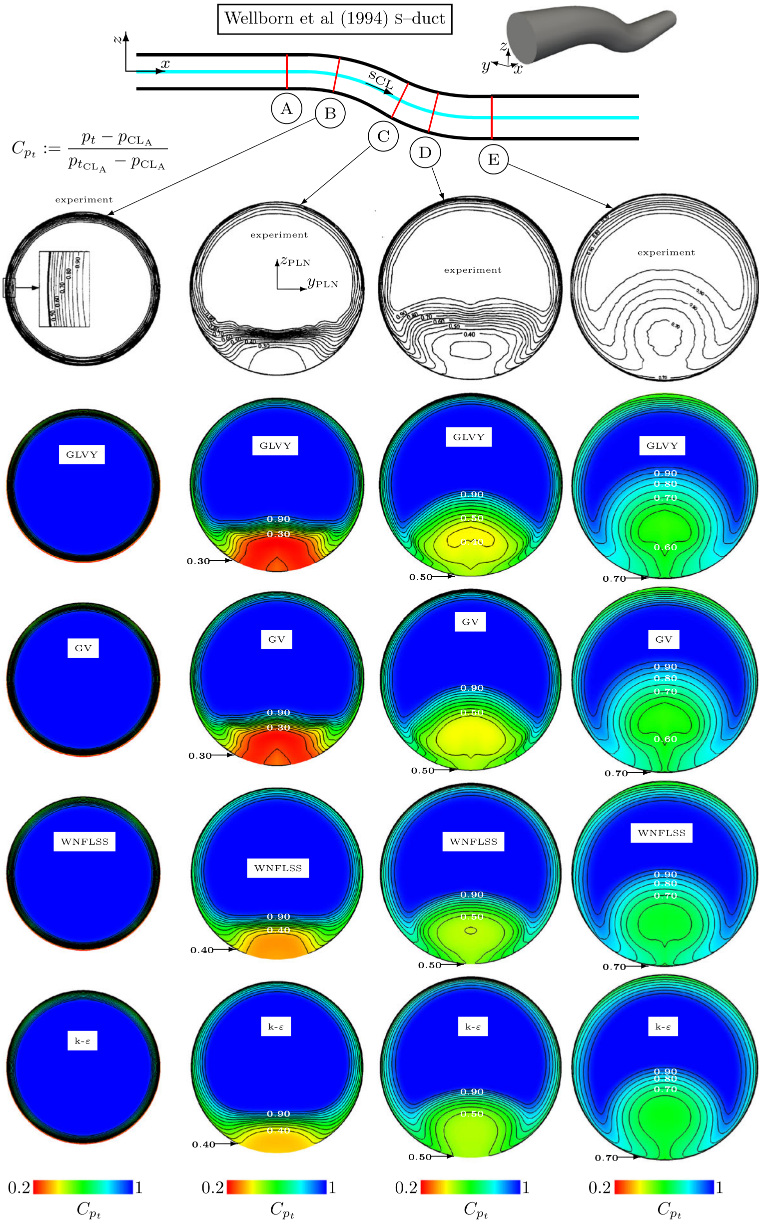

**Fig. 22** Comparison, at 4 measurement planes (planes ⊥ to the centerline define stations of circular cross-section), of experimental [80] contours of total pressure coefficient $C_{p_t}$ (based on centerline quantities at plane A; contour step 0.05), with computations ($2 \times 10^6$ points grid discretizing the entire duct; Table 2) using (Section 2.1) the GV [35], the WNF–LSS [29] and the GLVY [28] RSMs, and the LS [51] linear k–ε model ($Re_{\text{CL}_\text{A}} = 2.6 \times 10^6$, $\bar{M}_{\text{CL}_\text{A}} \approxeq 0.6$; Table 3)

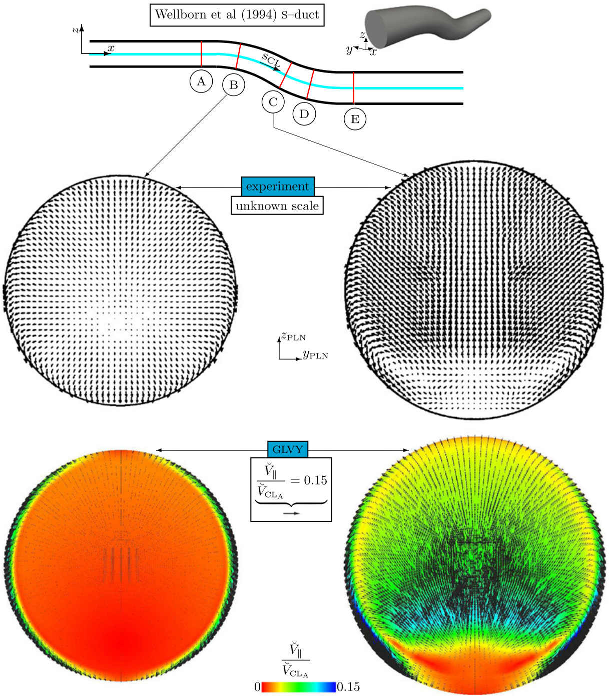

**Fig. 23** Comparison, at 2 measurement planes (planes ⊥ to the centerline define stations of circular cross-section), of experimental [80] vectors (unknown scale) of in-plane (secondary) velocity $\bar{\mathbf{V}}_{\|}$ (made nondimensional by the centerline velocity at plane A, $\check{V}_{\mathrm{CL_A}}$), with computations ($2 \times 10^6$ points grid discretizing the entire duct; Table 2) using (Section 2.1) the GLVY [28] RSM ($Re_{\mathrm{CL_A}} = 2.6 \times 10^6$, $\bar{M}_{\mathrm{CL_A}} \approxeq 0.6$; Table 3)

the linear LS k–$\varepsilon$ model predict a thinner ($z$-wise) low-speed region, with weak recirculation near the wall, and lower levels of k (Fig. 17).

The GLVY and GV RSMs' predictions compare quite well with experimental wall-pressure data (Figs. 18, 19), correctly predicting the pressure-plateau on the duct floor ($\phi_{\mathrm{EXP}} = 170$ deg; Fig. 18) and the significant $z$-wise extent of the low-speed region indicated by the presence of the pressure-plateau at duct midplane ($\phi_{\mathrm{EXP}} = 90$ deg; Fig. 18). This large separated flow region induces substantial flow blockage [16, pp. 310–311], accelerating the flow in the duct's ceiling area ($\phi_{\mathrm{EXP}} = 10$ deg; Fig. 18). The satisfactory agreement of the GLVY and GV RSMs' predictions with measurements near the duct ceiling ($\phi_{\mathrm{EXP}} = 10$ deg; Fig. 18) indicates that the GLVY and GV RSMs yield a satisfactory prediction of the blockage induced by the large separation on the duct floor (Fig. 17). Near the beginning of the S-bend, at planes A (one inlet radius $R_{\mathrm{CSG_1}}$ upstream) and B (approximately one inlet diameter $D_{\mathrm{CSG_1}}$ downstream), all 4 turbulence models are in excellent agreement with measurements (Fig. 19), correctly predicting in plane B the circumferential pressure-gradient that drives the boundary-layer fluid along the duct's circumference (Fig. 23) from ceiling (higher pressure due to the streamwise-concave wall; Fig. 19) to floor (lower pressure due to the streamwise-convex wall; Fig. 19). At plane C, in the separated flow region (Figs. 17, 18), the GLVY and GV RSMs are again in excellent agreement with

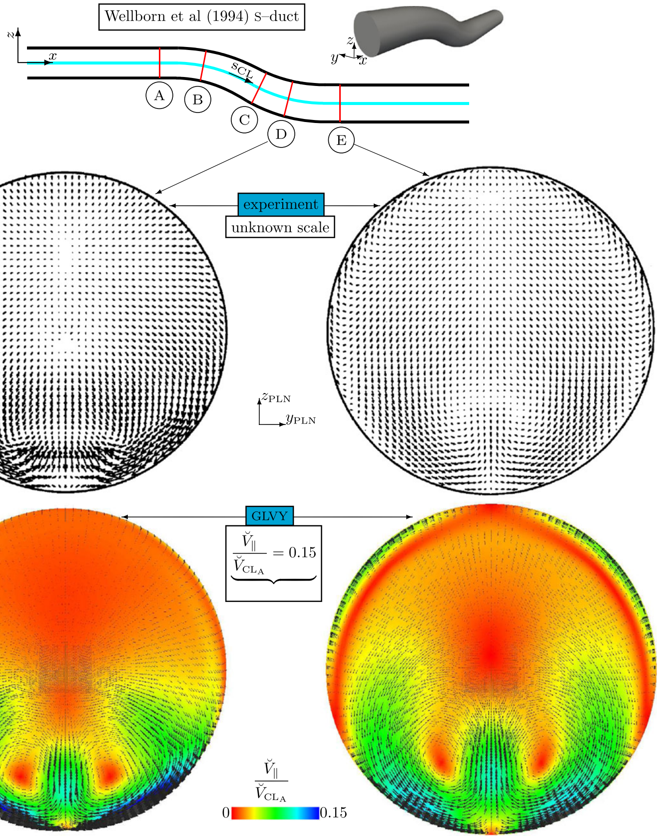

**Fig. 24** Comparison, at 2 measurement planes (planes ⊥ to the centerline define stations of circular cross-section), of experimental [80] vectors (unknown scale) of in-plane (secondary) velocity $\bar{\mathbf{V}}_{\parallel}$ (made nondimensional by the centerline velocity at plane A, $\breve{V}_{\mathrm{CL_A}}$), with computations ($2 \times 10^6$ points grid discretizing the entire duct; Table 2) using (Section 2.1) the GLVY [28] RSM ($Re_{\mathrm{CL_A}} = 2.6 \times 10^6$, $\bar{M}_{\mathrm{CL_A}} \approxeq 0.6$; Table 3)

measurements, correctly predicting the circumferential evolution of $C_p$ (Fig. 19) both in level and shape. The WNF–LSS RSM predicts the correct shape of the circumferential evolution of $C_p$ at plane C, but largely overestimates its value by ∼50 %, whereas the linear LS k–$\varepsilon$ model which overestimates $C_p$ even more fails to predict the inversion the circumferential pressure-gradient (Fig. 19) from channel mid-height ($\phi_{\mathrm{EXP}} \approxeq 110$ deg) to floor ($\phi_{\mathrm{EXP}} \approxeq 180$ deg). At plane D, where the flow reattaches in the experiment (Fig. 18), the GLVY and GV RSMs again provide the best prediction, compared to the WNF–LSS RSM and the linear LS k–$\varepsilon$ model, but they slightly overestimate $C_p$, especially near the floor (130 deg $\lessapprox \phi_{\mathrm{EXP}} \lessapprox$ 180 deg; Fig. 19).

Field pneumatic-probe measurements of $C_p$ (Fig. 20) at plane B indicate a slight static-pressure distortion which is not predicted by the computations (Fig. 20) and is not observed in the wall-pressure measurements (Fig. 19). At plane C, the GLVY and GV RSMs are in reasonable agreement with measurements, correctly predicting the flow acceleration near the ceiling (Fig. 20) induced by the floor-separation blockage (Figs. 17, 18). The WNF–LSS RSM which predicts separation downstream of experiment (Figs. 17, 18) severely overestimates $C_p$ at plane C (Fig. 20), the linear LS k–$\varepsilon$ model performing worse. At the near-reattachment plane D, the GLVY and GV RSMs are in good agreement with measurements, substantially outperforming the WNF–LSS RSM and the LS k–$\varepsilon$ closure (Fig. 20).

The velocity field, at each measurement plane, can be decomposed into a plane-normal component $\mathbf{V}_{\perp \text{PLN}}$ and an in-plane (parallel) component $\mathbf{V}_{\parallel \text{PLN}}$, $\mathbf{V} = \mathbf{V}_{\perp \text{PLN}} + \mathbf{V}_{\parallel \text{PLN}}$, where $\text{PLN} \in \{\text{A}, \text{B}, \text{C}, \text{D}, \text{E}\}$. The plane-normal mean-velocities $\breve{V}_{\perp}$ (Fig. 21) indicate the regions of separated and low-speed flow, which also correspond to the high-loss regions (low $C_{p_t}$; Fig. 22). The GLVY and GV RSMs are in overall satisfactory agreement with measurements (Figs. 21, 22) correctly predicting the backflow region at plane C and the flow blockage at the reattachment plane D and at the exit plane E (Fig. 21). As a consequence, the GLVY and GV RSMs also predict correctly the high level of loss in the backflow region (low $C_{p_t}$; plane C; Fig. 22) and the subsequent streamwise evolution of the high-loss region (planes D and E; Fig. 22). On the contrary, the linear LS k–$\varepsilon$ model, and to a lesser extent the WNF–LSS RSM, underpredict both backflow (Fig. 21) and losses (Fig. 22), predicting a less thick low-speed high-loss region everywhere (Figs. 21, 22).

The GLVY RSM (whose results are very close to those obtained with the GV RSM; Figs. 17–22), predicts quite satisfactorily the structure of secondary (in-plane $\mathbf{V}_{\parallel}$) flows (Figs. 23, 24). At plane B (Fig. 23), the circumferential pressure-gradient (Fig. 19) drives the boundary-layer flow from ceiling to floor along the duct walls (Fig. 23). At the separated-flow plane C (Fig. 23) this downward flow interacts with the large separation at the duct's floor (Fig. 17) forming 2 contrarotating vortices (Fig. 23), which lift off the floor as they are convected downstream (planes D and E; Fig. 24).

The differences in predictive accuracy between the 4 turbulence models (Figs. 17–22) is directly related to differences in the secondary-flow structure (Fig. 25). At plane B, where the flow is still attached (Fig. 21), all 4 turbulence closures yield quite similar results (Fig. 25). At the separated-flow plane C, GLVY and GV RSMs predict a thick low-$\breve{V}_{\parallel}$ region (Fig. 25), with distinct tails roughly marking the centers of 2 contrarotating vortices (Fig. 23), in good agreement with measurements. The WNF–LSS RSM predicts too thin a low-speed region (Fig. 25) and the 2 tails are less sharp, these 2 defaults being even more pronounced for the linear LS k–$\varepsilon$ model. The differences between the GLVY and GV RSMs on the one hand and the WNF–LSS RSM and the linear LS k–$\varepsilon$ closure on the other, are much more pronounced at the reattachment plane D (Fig. 25), where the 2 vortices have lifted off the floor in the GLVY and GV RSMs predictions (Fig. 25), in quite satisfactory agreement with measurements (Fig. 24), whereas they are more diffuse and closer to the wall in the WNF–LSS RSM predictions, which also underestimate the 2 symmetric high-$\breve{V}_{\parallel}$ regions near the duct floor (plane D; Figs. 24, 25). These high-$\breve{V}_{\parallel}$ regions are simply absent in the linear LS k–$\varepsilon$ model predictions (Fig. 25). At the exit plane E, the GLVY and GV RSMs predict sharp regions of low speed (Fig. 25) which correspond to the centers of the vortices (Fig. 24), with regions of high-$\breve{V}_{\parallel}$ near the ducts floor (Figs. 24, 25) and in the region between the 2 contrarotating vortices (Fig. 25), in good agreement with measurements. The vortices predicted by the WNF–LSS RSM and the linear k–$\varepsilon$ model are closer to the duct floor and their centers are less sharp (Fig. 25).

For the Wellborn et al. [80] test-case as for the previous ones (Sections 3.1 and 3.2), the GLVY and GV RSMs yield very similar results, and are in quite satisfactory agreement with measurements, showing that properly calibrated RSM–RANS closures can predict flows with large separation and wall-curvature effects. The GLVY and GV RSMs considerably

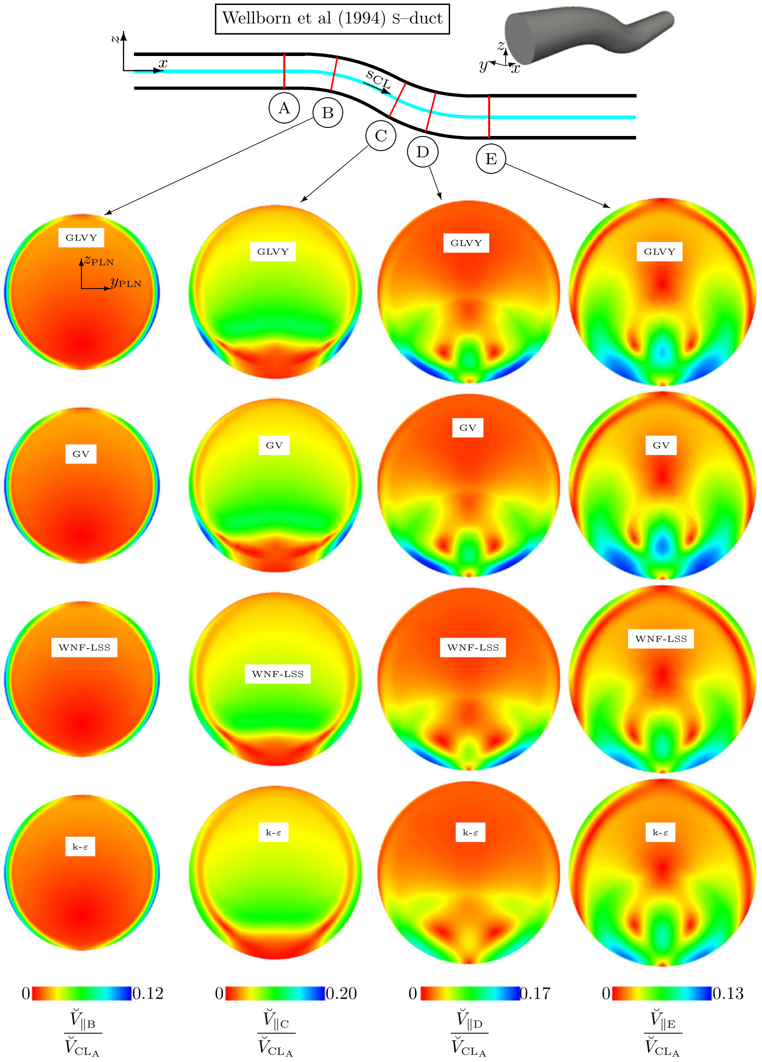

**Fig. 25** Level plots of the module of in-plane (secondary) velocity $\bar{\mathbf{V}}_{\parallel}$ (made nondimensional by the centerline velocity at plane A, $\check{V}_{\mathrm{CL_A}}$), at 4 measurement planes (planes ⊥ to the centerline define stations of circular cross-section), computed ($2 \times 10^6$ points grid discretizing the entire duct; Table 2) using (Section 2.1) the GV [35], the WNF–LSS [29] and the GLVY [28] RSMs, and the LS [51] linear k–$\varepsilon$ model ($Re_{\mathrm{CL_A}} = 2.6 \times 10^6$, $\bar{M}_{\mathrm{CL_A}} \approxeq 0.6$; Table 3)

outperform the WNF–LSS RSM, and this is again attributed to the $C_{\phi}^{(\mathrm{RH})}$ coefficient-function used (Table 1), because predictions of the Wellborn et al. [80] test-case using the GV and GV–DH (cf Section 3.1) RSMs are very similar one with another [77, Figs. 11–12, pp. 1153–1154], implying that the turbulent diffusion closure is less influential than pressure-strain redistribution in this flow. On the other hand, the improvement of the WNF–LSS RSM over the linear LS k–$\varepsilon$ model for this separation-dominated flow is weak.

## 4 Conclusions

In the present work, 3 wall-normal-free RSMs were assessed through comparison with experimental data for complex 3-D duct flows, highlighting the impact of the closure used for the velocity/pressure-gradient tensor $\Pi_{ij}$ (7) and for turbulent diffusion by the fluctuating velocities $d_{ij}^{(u)}$ (5) on the predictive accuracy of the models.

The Gessner and Emery [39] square duct flow is dominated by turbulence-anisotropy-driven secondary flows whereas the Davis and Gessner [19] C-to-R transition duct flow combines pressure-driven secondary flows in the transition section with turbulence-anisotropy-driven secondary flows in the straight constant cross-section exit part. Therefore, these test-cases are particularly useful in evaluating the predictive accuracy of turbulence closures for secondary flows where streamwise vorticity is important. Finally, the Wellborn et al. [80] diffusing S-duct contains a large region of separated flow and tests the ability of the turbulence models to accurately predict 3-D separation and reattachment in presence of blockage due to confinement and of secondary flows.

Results with the baseline LS [51] linear k–$\varepsilon$ closure were included as a reference for comparison with the more advanced differential RSMs. The underlying Boussinesq's hypothesis pathologically returns negligible levels of normal-stress anisotropy [82, pp. 273–279] and for this reason the LS k–$\varepsilon$ predicts negligibly weak ($\sim$0) secondary velocities both in the square-duct [39] and in the straight exit part of the C-to-R duct [19]. Furthermore, in the S-duct [80] test-case, the LS k–$\varepsilon$ model, which has been calibrated for equilibrium shear flows, severely underestimates separation. For all of the 3 test-cases the LS k–$\varepsilon$ closure compares very poorly with experimental data.

The WNF–LSS RSM [29] adopts the Launder-Shima [52] closure for the homogeneous part of $\Pi_{ij}$ and is therefore calibrated in zero-pressure-gradient flat-plate boundary-layer flow. As a consequence, it underestimates separation in the S-duct [80] test-case. On the other hand it has the differential RSMs' inherent ability to predict normal-stress anisotropy and performs quite well for the C-to-R duct [19] but underestimates the centerline velocity peak in the developing square-duct flow [39]; this inadequacy was traced to the cumulative influence of the homogeneous rapid redistribution isotropisation-of-production closure (7) $C_{\phi}^{(\text{RH})}$ (Table 1) and the Daly-Harlow turbulent-diffusion model (Table 1).

For all of the 3 test-cases that were examined [19, 39, 80], the GLVY [28] and GV [35] RSMs yield very similar results in quite satisfactory agreement with measurements, implying that the extra terms in the $\Pi_{ij}$ closure (7) used in the GLVY RSM (Table 1) have little influence for the secondary and/or separated 3-D flows studied in this paper; however, these extra terms were found to substantially improve the apparent transition behaviour of the model. The coefficient-function $C_{\phi}^{(\text{RH})}$ used in the GLVY and GV RSMs (Table 1) was calibrated with reference to flows with large separation [31, 35]. As a result, the GLVY and GV RSMs perform quite well in the S-duct [80] flow. They predict quite satisfactorily the other 2 test-cases [19, 39] as well, although they underpredict the strength of the secondary flow velocities and the level of the Reynolds-stress tensor anisotropy.

The results presented in the paper suggest that RSM RANS has the potential to predict complex 3-D flows with streamwise vorticity and separation. Further improvements in the prediction of the Reynolds-stress tensor anisotropy might be achieved by the use of a differential model for the full Reynolds-stress-dissipation tensor $\varepsilon_{ij}$ [28, 56]. Furthermore, the turbulence structure in separated and reattaching/relaxing flows exhibits strong hysteresis [20] whose inclusion in the model should be investigated [59].

Of course, variable resolution approaches [23, 48, 58], where only a part (unresolved [43, 44, 67, 76]) of the turbulent fluctuations is modelled, are a promising alternative for the simulation of realistic high-Reynolds number flows, with necessarily higher (in order-of-magnitude) computational costs because of the required time-consistency and of the simulation-time necessary for the convergence of statistics. All of these approaches are based on underlying transport-equation models for the unresolved stresses [12, 13] and can also benefit from the development of advanced RANS models of high predictive accuracy and equally from efficient and robust high-order-accurate solvers for Reynolds-stress transport [6].

**Acknowledgments** The present work was initiated within the DGA-funded research project CACV with Dassault-Aviation. The computations were performed using HPC ressources allocated at GENCI–IDRIS (Grants 2013– and 2014–020218) from ICS–UPMC (ANR–10–EQPX–29–01). The authors are listed alphabetically.

## References

1. Adams, J.C., Brainerd, W.S., Hendrickson, R.A., Maine, R.E., Martin, J.T., Smith, B.T.: The Fortran 2003 Handbook. Springer, New York (2009). doi:10.1007/978-1-84628-746-6
2. AERODYNAMICS: aerodynamics (a library and software package for computational aerodynamics). http://sourceforge.net/projects/aerodynamics (2015). (version 1.0.3)
3. Aloui, F., Berrich, E., Pierrat, D.: Experimental and numerical investigations of a turbulent flow behavior in isolated and nonisolated conical diffusers. ASME J. Fluids Eng. **133**, 011201 (2011). doi:10.1115/1.4003236
4. Anxionnaz-Minvielle, Z., Cabassud, M., Gourdon, C., Tochon, P.: Influence of the meandering channel geometry on the thermo-hydraulic performances of an intensified heat exchanger/reactor. Chem. Eng. Processing **73**, 67–80 (2013)
5. Atkins, H., Casper, J.: Nonreflective boundary conditions for high-order methods. AIAA J. **32**, 512–518 (1994)
6. Ben Nasr, N., Gerolymos, G.A., Vallet, I.: Low-diffusion approximate Riemann solvers for Reynolds-stress transport. J. Comp. Phys. **268**, 186–235 (2014). doi:10.1016/j.jcp.2014.02.010
7. Bradshaw, P.: Compressible turbulent shear layers. Ann. Rev. Fluid Mech. **9**, 33–54 (1977)
8. Bradshaw, P.: Turbulent secondary flows. Ann. Rev. Fluid Mech. **19**, 53–74 (1987)
9. Brundrett, E., Baines, W.D.: The production and diffusion of vorticity in duct flow. J. Fluid Mech. **19**, 375–394 (1964)
10. Chakravarthy, S.R.: Relaxation methods for unfactored implicit upwind schemes. In: AIAA Paper 1984–0165 (1984)
11. Chang, D., Tavoularis, S.: Numerical simulation of turbulent flow in a 37-rod bundle. Nucl. Eng. Des. **237**, 575–590 (2007)
12. Chaouat, B., Schiestel, R.: A new partially integrated transport model for subgrid-scale stresses and dissipation rates for turbulent developing flows. Phys. Fluids **17**(6), 065106 (2005)
13. Chaouat, B., Schiestel, R.: From single-scale turbulence models to multiple-scale and subgrid-scale models by fourier transform. Theor. Comp. Fluid Dyn. **21**, 201–229 (2007)
14. Chassaing, J.C., Gerolymos, G.A., Vallet, I.: Reynolds-stress model dual-time-stepping computation of unsteady 3-D flows. AIAA J. **41**(10), 1882–1894 (2003)
15. Craft, T.J., Launder, B.: Principles and performance of TCL-based second-moment closures. Flow Turb. Comb. **66**, 355–372 (2001)
16. Cumpsty, N.A.: Compressor Aerodynamics. Addison Wesley Longman, Essex[GBR] (1989)
17. Daly, B.J., Harlow, F.H.: Transport equations in turbulence. Phys. Fluids **13**, 2634–2649 (1970)
18. Davis, D.O.: Experimental investigation of turbulent flow through a circular-to-rectangular transition duct. PhD, University of Washington, Seattle [ WA, USA].(also NASA–TM–105210) (1991)
19. Davis, D.O., Gessner, F.B.: Experimental investigation of turbulent flow through a circular to rectangular duct. AIAA J. **30**(2), 367–375 (1992)
20. Délery, J.M.: Experimental investigation of turbulence properties in transonic shock/boundary-layer interactions. AIAA J. **21**, 180–185 (1983). (also AIAA Paper 1981–1245, 1981)

21. Délery, J.M.: Robert Legendre and Henri Werlé: Toward the elucidation of 3-D separation. Ann. Rev. Fluid Mech. **33**, 129–154 (2001)
22. Demuren, A.O.: Calculation of turbulence-driven secondary motion in ducts with arbitrary cross section. AIAA J. **29**(4), 531–537 (1991)
23. Egorov, Y., Menter, F.R., Lechner, R., Cokljat, D.: The scale-adaptive simulation method for unsteady turbulent flow predictions — ii — application to complex flows. Flow Turb. Comb. **85**, 139–165 (2010)
24. ERCOFTAC: European Research Community on Flow, Turbulence and Combustion Database: Classic Collection. http://cfd.mace.manchester.ac.uk/ercoftac/ (1999). Accessed 5 Nov 2014
25. Fujii, S., Okiishi, T.H.: Curved diffusing annulus turbulent boundary-layer development. J. Aircraft **9**(2), 97–98 (1972)
26. Gerolymos, G.A., Joly, S., Mallet, M., Vallet, I.: Reynolds-stress model flow prediction in aircraft-engine intake double-S-shaped duct. J. Aircraft **47**(4), 1368–1381 (2010). doi:10.2514/1.47538
27. Gerolymos, G.A., Lo, C., Vallet, I.: Tensorial representations of reynolds-stress pressure-strain redistribution. ASME J. Appl. Mech **79**(4), 044506 (2012). doi:10.1115/1.4005558
28. Gerolymos, G.A., Lo, C., Vallet, I., Younis, B.A.: Term-by-term analysis of near-wall second moment closures. AIAA J. **50**(12), 2848–2864 (2012). doi:10.2514/1.J051654
29. Gerolymos, G.A., Sauret, E., Vallet, I.: Contribution to the single-point-closure Reynolds-stress modelling of inhomogeneous flow. Theor. Comp. Fluid Dyn **17**(5–6), 407–431 (2004a)
30. Gerolymos, G.A., Sauret, E., Vallet, I.: Influence of inflow-turbulence in shock-wave/turbulent-boundary-layer interaction computations. AIAA J. **42**(6), 1101–1106 (2004b)
31. Gerolymos, G.A., Sauret, E., Vallet, I.: Oblique-shock-wave/boundary-layer interaction using near-wall Reynolds-stress models. AIAA J. **42**(6), 1089–1100 (2004c)
32. Gerolymos, G.A., Sénéchal, D., Vallet, I.: Wall effects on pressure fluctuations in turbulent channel flow. J. Fluid Mech **720**, 15–65 (2013). doi:10.1017/jfm.2012.633
33. Gerolymos, G.A., Tsanga, G.: Biharmonic 3-D grid generation for axial turbomachinery with tip-clearance. J. Prop. Power **15**(3), 476–479 (1999)
34. Gerolymos, G.A., Vallet, I.: Implicit computation of the 3-D compressible Navier-Stokes equations using $k-\varepsilon$ turbulence closure. AIAA J. **34**(7), 1321–1330 (1996)
35. Gerolymos, G.A., Vallet, I.: Wall-normal-free near-wall Reynolds-stress closure for 3-D compressible separated flows. AIAA J. **39**(10), 1833–1842 (2001)
36. Gerolymos, G.A., Vallet, I.: Mean-flow-multigrid for implicit reynolds-stress-model computations. AIAA J. **43**(9), 1887–1898 (2005)
37. Gerolymos, G.A., Vallet, I.: Implicit mean-flow-multigrid algorithms for Reynolds-stress-model computations of 3-D anisotropy-driven and compressible flows. Int. J. Num. Meth. Fluids **61**(2), 185–219 (2009). doi:10.1002/fld.1945
38. Gerolymos, G.A., Vallet, I.: Pressure, density, temperature and entropy fluctuations in compressible turbulent plane channel flow. J. Fluid Mech. **757**, 701–746 (2014). doi:10.1017/jfm.2014.431
39. Gessner, F.B., Emery, A.F.: The numerical prediction of developing turbulent flow in rectangular ducts. ASME J. Fluids Eng **103**, 445–455 (1981). doi:10.1080/10618562.2013.772984
40. Gessner, F.B., Jones, J.B.: On some aspects of fully-develped turbulent flow in rectangular channels. J. Fluid Mech. **23**, 689–713 (1965)
41. Gessner, F.B., Po, J.K., Emery, A.F.: Measurements of developing turbulent flow in a square duct. In: Durst, F., Launder, B.E., Schmidt, F.W., Whitelaw, J.H. (eds.) Turbulent Shear Flows I — Selected Papers from the 1. International Symposium on Turbulent Shear Flows, The Pennsylvania State University, University Park, Pennsylvania, USA, April 18–20, 1977, pp. 119–136 Springer, Berlin [DEU] (1979)
42. Gibson, M.M., Launder, B.E.: Ground effects on pressure fluctuations in the atmospheric boundary-layer. J. Fluid Mech. **86**, 491–511 (1978)
43. Girimaji, S.S.: Partially-averaged navier-stokes model for turbulence: a reynolds-averaged navier-stokes to direct numerical simulation bridging method. ASME J. Appl. Mech. **73**, 422–429 (2006)
44. Girimaji, S.S., Jeong, E., Srinivasan, R.: Partially-averaged navier-stokes method for turbulence: fixed point analysis and comparison with unsteady partially averagde navier-stokes. ASME J. Appl. Mech. **73**, 413–421 (2006)
45. Hanjalić, K.: Advanced turbulence closure models: A view of current status and future prospects. Int. J. Heat Fluid Flow **15**, 178–203 (1994)
46. Hanjalić, K., Launder, B.E.: Contribution towards a Reynolds-stress closure for low-reynolds-number turbulence. J. Fluid Mech **74**, 593–610 (1976)
47. Harloff, G.J., Smith, C.F., Bruns, J.E., DeBonis, J.R.: Navier-Stokes analysis of three-dimensional s-ducts. J. Aircraft **30**(4), 526–533 (1993)

48. Jakirlić, S., Maduta, R.: Extending the bounds of steady rans closures: Toward an instability-sensitive reynolds-stress model. Int. J. Heat Fluid Flow **51**, 175–194 (2015)
49. Jiang, G.S., Shu, C.W.: Efficient implementation of weighted ENO schemes. J. Comp. Phys. **126**, 202–228 (1996)
50. Kovasznay, L.S.G., Kibens, V., Blackwelder, R.F.: Large-scale motion in the intermittent region of a turbulent boundary-layer. J. Fluid Mech. **41**, 283–325 (1970)
51. Launder, B.E., Sharma, B.I.: Application of the energy dissipation model of turbulence to the calculation of flows near a spinning disk. Lett. Heat Mass Transfer **1**, 131–138 (1974)
52. Launder, B.E., Shima, N.: 2-moment closure for the near-wall sublayer: Development and application. AIAA J. **27**(10), 1319–1325 (1989)
53. Leschziner, M.A.: Turbulence modelling for separating flows with anisotropy-resolving closures. Phil. Trans. Roy. Soc. London A **358**, 3247–3277 (2000)
54. Lien, F.S., Leschziner, M.A.: Second moment closure for 3-D turbulent flow around and within complex geometries. Comp. Fluids **25**, 237–262 (1996)
55. Lumley, J.L.: Computational modeling of turbulent flows. Adv. Appl. Mech. **18**, 123–176 (1978)
56. Lumley, J.L., Yang, Z., Shih, T.H.: A length-scale equation. Flow Turb. Comb. **63**, 1–21 (1999)
57. Mansour, N.N., Kim, J., Moin, P.: Reynolds-stress and dissipation-rate budgets in a turbulent channel flow. J. Fluid Mech **194**, 15–44 (1988)
58. Menter, F.R., Egorov, Y.: The scale-adaptive simulation method for unsteady turbulent flow predictions — i — theory and model description. Flow Turb. Comb. **85**, 113–138 (2010)
59. Olsen, M.E., Coakley, T.J.: The lag model, a turbulence model for nonequilibrium flows. AIAA Paper, 2001–2564 (2001)
60. Österlund, J.M., Johansson, A.V., Nagib, H.M., Hites, M.H.: A note on the overlap region in turbulent boundary-layers. Phys. Fluids **12**(1), 1–4 (2000)
61. Po, J.K.: Developing turbulent flow in the entrance region of a square duct. MSc, Washington University, Seattle (1975)
62. Reichert, B.A.: A study of high-speed flows in an aircraft transition duct. PhD, Iowa State University, Ames (1991). (also NASA–TM–104449)
63. Reif, B.P., Andersson, H.I.: Prediction of turbulence-generated secondary mean flow in a square duct. Flow Turb. Comb **68**, 41–61 (2002)
64. Rumsey, C.L.: Apparent transition behavior of widely-used turbulence models. Int. J. Heat Fluid Flow **28**, 1460–1471 (2007)
65. Rumsey, C.L.: Consistency, verification, and validation of turbulence models for reynolds-averaged navier-stokes applications. IMechE J. Aerosp. Eng. **224**(11), 1211–1218 (2010)
66. Sauret, E., Vallet, I.: Near-wall turbulent pressure diffusion modelling and influence in 3-D secondary flows. ASME J. Fluids Eng. **129**(5), 634–642 (2007)
67. Schiestel, R., Dejoan, A.: Towards a new partially integrated transport model for coarse grid unsteady turbulent flow simulations. Theor. Comp. Fluid Dyn. **18**, 443–468 (2005)
68. Shima, N.: Prediction of turbulent boundary-layer flows with a 2-moment closure — Part 1 — Effects of periodic pressure gradient, wall transpiration, and free-stream turbulence. ASME J. Fluids Eng. **115**, 56–63 (1993)
69. Simpson, R.L.: Turbulent boundary-layer separation. Ann. Rev. Fluid Mech. **21**, 205–234 (1989)
70. Smits, A.J., Young, S.T.B., Bradshaw, P.: The effect of high surface curvature on turbulent boundary-layers. J. Fluid Mech. **94**, 209–242 (1979)
71. So, R.M.C., Mellor, G.L.: Turbulent boundary-layers with large stramline curvature effects. J. Appl. Math. Phys. **29**, 54–74 (1978)
72. So, R.M.C., Yuan, S.P.: A geometry independent near-wall Reynolds-stress closure. Int. J. Eng. Sci. **37**, 33–57 (1999)
73. Sotiropoulos, F., Patel, V.C.: Prediction of turbulent flow through a transition duct using a 2-moment closure. AIAA J. **32**(11), 2194–2204 (1994)
74. Sotiropoulos, F., Patel, V.C.: Application of Reynolds-stress transport models to stern and wake flows. J. Ship Res. **39**(4), 263–283 (1995)
75. Sotiropoulos, F., Patel, V.C.: Turbulence anisotropy and near-wall modeling in predicting 3-D shear flows. AIAA J. **33**(3), 504–514 (1995)
76. Speziale, C.G.: Turbulence modeling for time-dependent RANS and VLES: A review. AIAA J. **36**(2), 173–184 (1998)
77. Vallet, I.: Reynolds-stress modelling of 3-D secondary flows with emphasis on turbulent diffusion closure. ASME J. Appl. Mech. **74**(6), 1142–1156 (2007)
78. Vallet, I.: Reynolds-stress modelling of $M = 2.25$ shock-wave/turbulent-boundary-layer interaction. Int. J. Num. Meth. Fluids **56**(5), 525–555 (2008)

79. Wellborn, S.R., Okiishi, T.H., Reichert, B.A.: A study of compressible flow through a diffusing S-duct. In: Techenical Mem. NASA–TM–1993–106411, NASA, Lewis Research Center, Cleveland [OH, USA] (1993)
80. Wellborn, S.R., Reichert, B.A., Okiishi, T.H.: Study of the compressible flow in a diffusing S-duct. J. Prop. Power **10**(5), 668–675 (1994)
81. White, M.F. Viscous Fluid Flow, 2nd edn. McGraw-Hill, New York (1991)
82. Wilcox, D.C. Turbulence Modelling for CFD, 2nd edn. DCW Industries, California, USA (1998)
83. Yakinthos, K., Vlahostergios, Z., Goulas, A.: Modeling the flow in a 90° rectangular duct using 1 Reynolds-stress and 2 eddy-viscosity models. Int. J. Heat Fluid Flow **29**, 35–47 (2008)